이학 석사 학위논문

TEMPLATED SYNTHESIS OF MESOPOROUS 3D CUBIC METAL ARCHITECTURES FROM THE SELF-ASSEMBLY OF BLOCK COPOLYMERS

블록공중합체의 자기조립을 통한 메조기공성 3차원 입방체 금속재료의 주형합성

2020년 8월

서울대학교 대학원

화학부 고분자화학 전공

이 희 림

TEMPLATED SYNTHESIS OF MESOPOROUS 3D CUBIC METAL ARCHITECTURES FROM THE SELF-ASSEMBLY OF BLOCK COPOLYMERS

지도교수 김 경 택

이 논문을 이학석사 학위논문으로 제출함

2020년 7월

서울대학교 대학원

화학부 고분자화학 전공

이 희 림

이희림의 석사 학위논문을 인준함

2020년 7월

위 원 장	최 태 림	(인)
부 위 원 장	김 경 택	(인)
위 원	손 병 혁	(인)

ABSTRACT

TEMPLATED SYNTHEIS OF MESOPOROUS 3D CUBIC METAL ARCHITECTURES FROM THE SELF-ASSEMBLY OF BLOCK COPOLYMERS

Heelim Lee

Department of Chemistry, Polymer Chemistry Major

The Graduate School

Seoul National University

Inspired by mathematicians and structural biologists who have defined and discovered periodic minimal surfaces that do not self-intersect, many chemists and material scientists have designed unique molecules that self-assemble into complex structures having a periodic array of nano- to mesosized pores and two non-intersecting internal channels. Structural transcription of such structures onto a variety of solid-state materials through templated synthesis has provided a versatile platform in preparing advanced materials having increased mass transport, specific activity, and stability.

Yet only one of the three most prevalent periodic cubic structures that appear in nature (Schwarz D, G, and P surfaces) has been explored extensively for imparting structure-driven performance enhancement to a material. In this research, the two other structures (the Schwarz P and D surface) are utilized in synthesizing

mesoporous cubic nickel, platinum, and gold particles and monoliths having periodic, interconnected, crystalline cubic structures by a simple two-step chemical reduction under mild conditions without energy-intensive calcination and electroplating procedures.

Since nickel substrates have been actively utilized as a template for chemical vapor deposition of carbon species, the nickel mesostructures synthesized here provide an access to a new type of carbon allotropes having a negative Gaussian curvature. Also, nickel has been widely sought as an inexpensive catalyst that can replace much rare and more expensive noble metals. Therefore, the mesoporous cubic nickel particles synthesized here opens new opportunities for developing catalysts having unique structures. Platinum catalysts having unique structures have been actively explored by research scientists, so the mesoporous cubic platinum particles synthesized here adds to the library for further research. The structural difference of this new structure compared to the famous gyroidal materials will be more pronounced in their plasmon absorbance behavior. Therefore, mesoporous cubic gold particles are synthesized and characterized.

This research contributes to the discovery of unique characteristics that the Schwarz P and D surfaces bring to metallic materials, which have not been actively researched in literature.

……

Keywords : templated synthesis, self-assembly, amphiphiles, block copolymers, mesostructure, metal plating, material chemistry

Student Number : 2017-26761

TABLE OF CONTENTS

LIST OF FIGURES

LIST OF TABLES

LIST OF SCHEMES

LIST OF ABBREVIATIONS

ATRP	atomic transfer radical polymerization
BCP	block copolymer
CV	cyclic voltammetry
CVD	chemical vapor deposition
DP_n	degree of polymerization (n)
EDC	1-Ethyl-3-(3-dimethylaminopropyl)carbodiimide
EDX	energy dispersive x-ray spectroscopy
FESEM	field-emission scanning electron microscopy
GPC	gel permeation chromatography
HRTEM	high-resolution transmission electron microscopy
MALDI	matrix-assisted laser desorption ionization
MC	dichloromethane
M_n	number average molecular weight
MS	mass spectroscopy
M_w	weight average molecular weight
NMR	nuclear magnetic resonnance
ORR	oxygen reduction reaction
PDI	polydispersity index
PEG	polyethylene glycol
$(PEG)_3$-*b*-PS	poly(ethylene glycol)$_3$-*block*-poly(styrene)
PMDETA	N,N,N′,N″,N″-Pentamethyldiethylenetriamine
PS	polystyrene
PTFE	polytetrafluoroethylene
RH	relative humidity
SDEMS	solvent diffusion-evaporation mediated self-assembly

SEM	scanning electron microscopy
TEM	transmission electron microscopy
THF	tetrahydrofuran
TOF	time of flight
TPMS	triply periodic minimal surface
WAXS	wide-angle x-ray spectroscopy

CHAPTER 1: INTRODUCTION

1.1 Triply periodic minimal surfaces (TPMS)

Triply periodic minimal surfaces (TPMS) refer to a surface that has zero mean curvature ($H = (\kappa_1+\kappa_2) / 2 = 0$, where κ_1 and κ_2 are the principle curvatures) at all points and has a unit structure repeated in a three-dimensional space. The first five non-trivial TPMS were introduced by a German mathematician Hermann Amandus Schwarz in 1883 (the Schwarz D, P, H, T, and CLP surfaces), rediscovering the D surface described by Bernhard Riemann in 1853.[1–3] A major addition to the library of TPMS was the 12 more surfaces described by Alan Hugh Schoen in 1970.[4] Over the following decades, variety of TPMS have been discovered and studied by mathematicians, physicists, and material scientists.[3–4] Few examples of TPMS are shown in **Figure 1**, including Lidinoid described by Sven Lidin and Stefan Larsson in 1990.[5] The discovery of such surfaces in nature, for example, in crystal inorganic and metal solids, cellular membranes, and biopolymers, in the late 1900s had triggered much scholarly attention.[3,6]

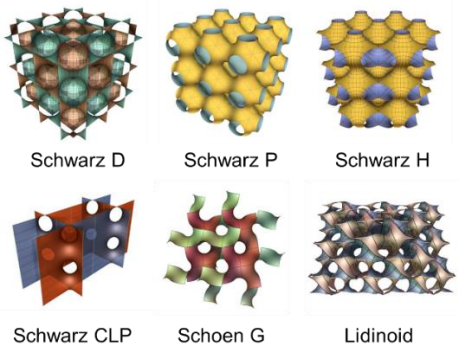

Figure 1. The 3D illustrations of the first few TPMS discovered by H. A. Schwarz, A. H. Schoen, and S. Lidin.[5,7]

Of particular interest in materials research has been bicontinuous cubic structures having a surface that divides the 3D space into two equal sub-volumes that do not self-intersect, namely, the Schwarz P (primitive cubic, space group $Im\bar{3}m$), D (diamond, space group $Pn\bar{3}m$), and G (gyroid, space group $Ia\bar{3}d$) surfaces. The most noticeable structural difference between the three is the number of struts that form a junction of the channels in each sub-volume, as illustrated in **Figure 2**. There are three, four, or six struts forming a junction along the channels of Schoen G, Schwarz D, and P surfaces, respectively.

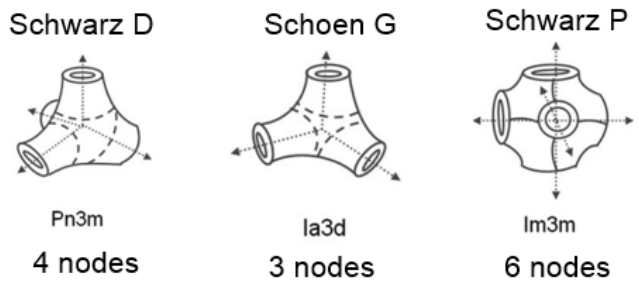

Figure 2. The schematic drawings of the three TPMS that are found as bicontinuous inverse cubic phases upon the self-assembly of amphiphiles.[9]

Another major difference between the three structures is that the P and D surfaces divide the 3D space into two congruent labyrinths (*i.e.* the two sub-volumes are identical by translation), while the G surface yields two incongruent labyrinths.[6] One could describe the difference in terms of the structural relationship between the three surfaces. The P and D surfaces are at ninety degrees Bonnet rotations of each other (*i.e.* associate family),[6–8] sharing negative Gaussian curvature ($K = \kappa_1 \cdot \kappa_2 < 0$), zero mean curvature (H), lengths and angles (**Figure 3**). The G surface is obtained at

about 38.0 degrees Bonnet rotations from the D surface,[6–8] therefore the G surface can be seen as an intermediate between the D and P surface.

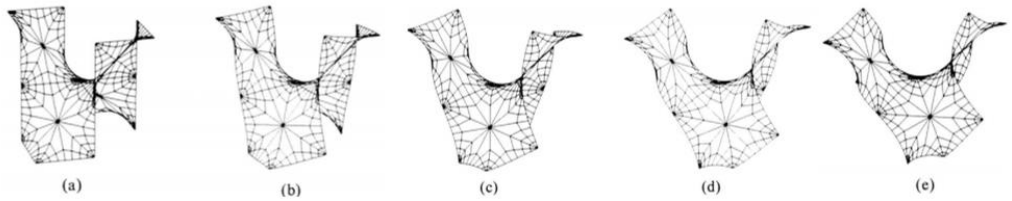

Figure 3. Bending of the D surface to the G surface (Bonnet transformation) at angles (a) 0°, (b) 10°, (c) 20°, (d) 30°, and (3) 38.015°. The flat points change from forming a fcc lattice (Schwarz D) to a bcc lattice (Schwarz P).[5]

The D, P, and G surface frequently appears in nature, for example, on butterfly wing scales, and in cellular organelles such as the endoplasmic reticulum.[9-10] The self-assembly of lipid molecules into the complex structures[11–14] is known to facilitate critical biological functions and properties such as cell fusion,[15,16] food digestion,[17,18] and biomolecule transport.[19] The underlying principles governing the self-assembly of lipid molecules in biological systems[20–21] have inspired synthetic chemists in designing unique liquid crystals[22–23] and block copolymer (BCP)[24–30] molecules that self-assemble into such complex structures. The incompatibility of different parts of an amphiphilic molecule (*e.g.* hydrophilic block and hydrophobic block) in a given environment induces thermodynamic phase separation that leads to the formation of unique structures.[31–33] Other than natural monooleins that appear in lipid membranes (**Figure 4a–c**), synthetic liquid crystals (**Figure 4d and 4e**) and block copolymers (**Figure 4f–i**) have demonstrated phase transition into the bicontinuous inverse cubic phases under bulk, solution, and thin-film self-assembly

conditions. Since block copolymers are easy to design and synthesize to prepare porous materials in nano to meso scale, polymer chemists have designed molecules having different microstructures, such as linear diblock copolymers, triblock copolymers, star-shaped, and dendritic block copolymers.

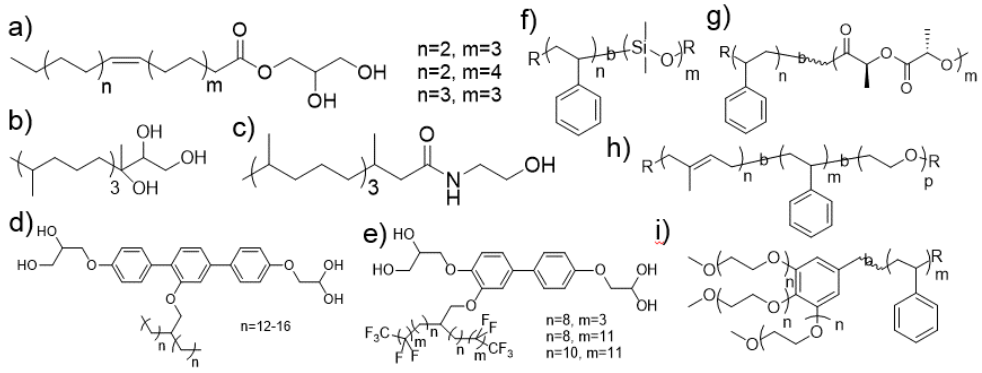

Figure 4. Exemplary molecules that self-assemble into bicontinuous cubic structures. a) monoolein, monopalmitolein, and monovaccenin[21]; b) phytantriol[21]; c) phytanoyl monoethanolamide[21]; d and e) thermotropic liquid cystals[22,23]; f) poly(styrene)-*b*-poly(dimethylsiloxane)[24]; g) poly(styrene)-*b*-poly(L-lactide)[25]; h) poly(isoprene)-*b*-poly(styrene)-*b*-poly(ethylene oxide)[26]; i) dendritic poly(ethylene glycol)$_3$-*b*-poly(styrene).[27–30]

1.2 Templated synthesis in materials chemistry

For the past two decades, tuning the performance of a material with structural characteristics has been an active topic of research. Ensinger et al.[34] generated 3D interconnected nanowires by electroplating platinum on a polycarbonate substrate that contains interconnected 3D networks prepared by etching a bulk substrate with high-energy gold ion beam (**Figure 5a**). The resulting polycrystalline platinum

nanowires have periodic lattice size of few hundreds of nanometers and an average wire diameter of 30 nanometers. Compared to commercially available platinum nanoparticle catalysts fixed on a carbon support, the platinum nanowires exhibit three times higher peak current density for methanol oxidation reaction while retaining the electrochemically active surface area over 500 CV cycles. Braun et al.[35] employed opal structure of stacked monodisperse polystyrene beads to impart inverse opal structure to an electrode that contains active cathode material plated by electrodepositing (**Figure 5b**). The resulting lithium or nickel cathode functions as a bulk battery electrode that shows upto 400 C or 1000 C charging/discharging rates with little capacity loss, benefiting from the 3D bicontinuous nanoarchitecture that facilitates rapid ion and electron transport paths.[35] Jaramillo et al.[36] prepared a double gyroid structure with an ABA-type poly(ethylene oxide)$_{19}$-*b*-poly(propylene oxide)$_{43}$-*b*-poly(ethylene oxide)$_{19}$ surfactant with tetrasilane precursor (**Figure 5c**). The prepared template is calcined at 400^{o}C for 4 hours, leaving the calcined silica template only. The silica template was subjected to platinum electroplating, and subsequent etching with 2% hydrofluorine leaves the gyroid platinum particles. The resulting material shows two-fold greater specific activity with lower overpotential required for oxygen reduction reaction (ORR), while retaining its stability over 10,000 cycles.

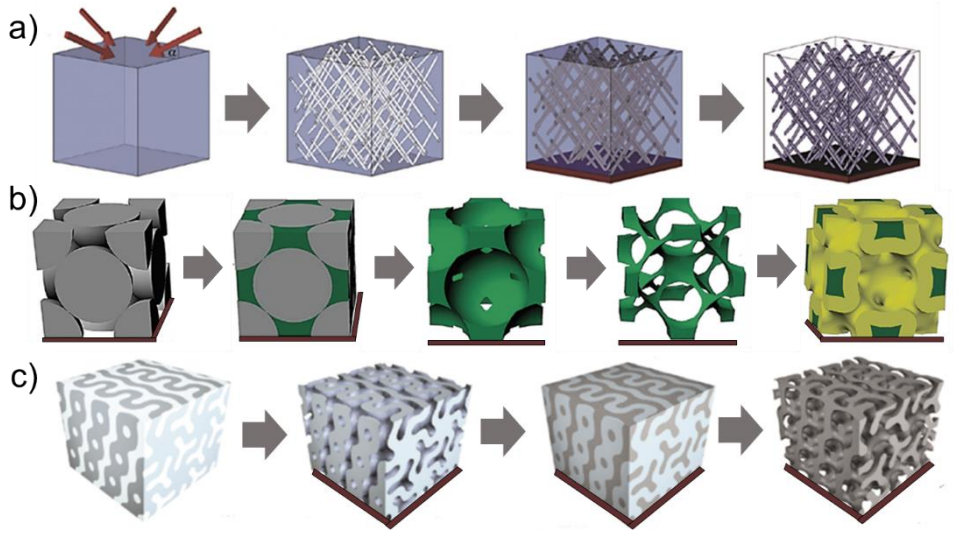

Figure 5. Templated synthesis of interconnected 3D metal networks. a) A bulk polycarbonate template is etched with Au or U ion beam (11 MeV/u) and the resulting porous template is subjected to electroplating of platinum.[34] b) Opal structure formed by stacked monodisperse polystyrene beads was used to translate inverse opal structure onto a cathode by electroplating.[35] c) Double gyroid structure prepared from poly(ethylene oxide)$_{19}$-*b*-poly(propylene oxide)$_{43}$-*b*-poly(ethylene oxide)$_{19}$ surfactant with tetrasilane precursor was used to translate single gyroid structure onto a platinum electrode by electroplating.[36]

Solar cells,[37] supercapacitors,[38,39] precious or inexpensive metal catalysts[36] and electrodes[35] that have a periodic, bicontinuous gyroid structure have demonstrated enhanced material performance, such as high peak external quantum efficiency and overall power conversion efficiency, and high specific capacitance combined with electrochromic color change functions. Such materials have benefited from much higher accessible substrate area,[40] increased mass transport and the uniform interconnectivity of the substructures. Most of the synthetic schemes include plating a metal electrode on the substrate for electroplating a desired metal on the

surface of the porous templates, which then has to be removed and replaced with relevant material when integrating a functioning device. Since the self-assembled structures cannot be retained during most of the electrochemical plating procedures, the structure has to be transferred onto an inorganic material by infiltration of the precursors and calcination at high temperatures.

The whole procedure for plating metal on a porous template can be simplified to a two-step procedure, activation and growth, first introduced by Funaki et al. in 1997.[41] A multivalent primary metal ion coordinates onto the electron-rich functional groups exposed to the surface of the porous template. The template is then immersed in a reductant solution, where the reductant molecules provide electrons to the pre-coordinated primary metal ions and reduce them to atomic metal, likely forming a group of metal clusters. The activated template is then immersed in a plating solution composed of a desirable secondary metal ion and a reductant, where the solution is stabilized with ammonia to provide a favorable reduction condition according to Pourbaix diagram and to prevent formation of undesirable species in the background. The electrons are exchanged between the primary metal and the secondary metal ions and the atomized metal clusters act as a site for further reduction (*i.e.* autocatalytic plating). The exchange of electrons between the primary and secondary metal is likely mediated by galvanic exchange, or the difference in their electrochemical potential. Therefore, the same principles should be able to work for a proper choice of the activating and growing metal pairs. Some pairs have been explored by few chemists.[42–45] It is also noting that the atomization of metal ions is a thermodynamic process, as the free energy of forming a new surface will have to be compensated. Also, the

kinetics take account as there are differences between the surfaces inside and outside of the porous templates.

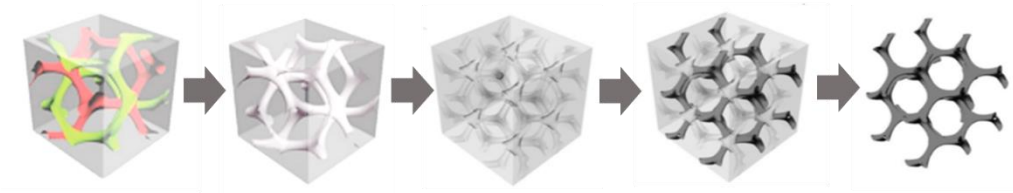

Figure 6. Templated synthesis of 3D cubic metal architecture by simple two-step chemical reduction. A double gyroid template is prepared from the self-assembly of poly(styrene)-*b*-poly(L-lactide), where hydrolysis of the PLLA block leaves the porous template available for electroless plating.[42-45]

1.3 Cubic Structures having Schwarz P and D surface

The three D, G, and P inverse cubic mesophases share a negative Gaussian curvature ($K= \kappa_1 \cdot \kappa_2 < 0$), which has caught the attention of material scientists and physical chemists recently. The discovery of C_{60} buckminsterfullerene ("buckyballs") having a positive Gaussian curvature by R. E. Smalley, R. F. Curl, and H. W. Kroto in 1985[46] (**Figure 7a**), and the isolation of graphene by A. Geim and K. Novoselov in 2004[47] having zero Gaussian curvature (**Figure 7b**) have led numerous breakthroughs in material science. A new type of carbon allotropes analogous to the Schwarz surfaces having a negative Gaussian curvature was first imagined by H. Terrones and A. L. Mackay in 1991,[48] which was put into a detailed calculation by Elser et al. in 1992[48] (**Figure 7c**). It is only recent that these carbon Schwarzites are attracting serious interests in the field.[50–53]

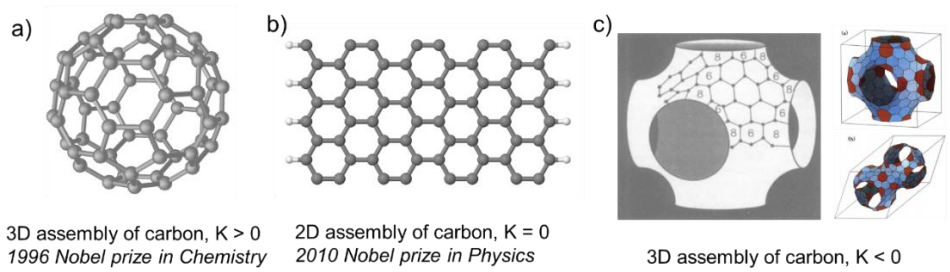

Figure 7. Different carbon allotropes in terms of Gaussian curvature ($K = \kappa_1 \cdot \kappa_2$). a) C_{60} buckminsterfullerene ("buckyballs") discovered by R. E. Smalley, R. F. Curl, and H. W. Kroto in 1985[46]; b) Graphene isolated from graphite by A. Geim and K. Novoselov in 2004[47]; c) Carbon Schwarzites proposed by H. Terrones and A. L. Mackay in 1991[48] and Elser et al. in 1992.[50]

Nickel is often used as a support for deposition of carbon species, for example, by chemical vapor deposition (CVD). Templated synthesis of metallic nickel that resembles the Schwarz P or D structure will provide an access to creating new carbon allotropes analogous to the Schwarz P or D structure. By self-assembly of branched-linear $(PEG)_3$-*b*-PS BCPs in a dilute solution or by solvent diffusion-evaporation mediated self-assembly (SDEMS),[27–30] structurally well-defined mesoporous templates that resemble the Schwarz D structure as colloidal particles (cubosomes, radius of few 10s of μm) or monoliths (thickness of few 100s of μm) were prepared (**Figure 8a**). By adopting the procedures available in the literature[42,45] and optimizing the plating conditions, mesoporous cubic nickel particles and cubic nickel monoliths were prepared (**Figure 8b and 8c**) by the two-step procedure of *in situ* chemical metal reduction on the surface of the porous template. Templated synthesis of mesoporous 3D cubic architectures for other transition metals, platinum and gold, were also demonstrated, adopting the procedures reported in the

literature.[43,44] This research provides opportunities to investigate the unique characteristics that the Schwarz D surfaces will bring to mesoporous metal materials.

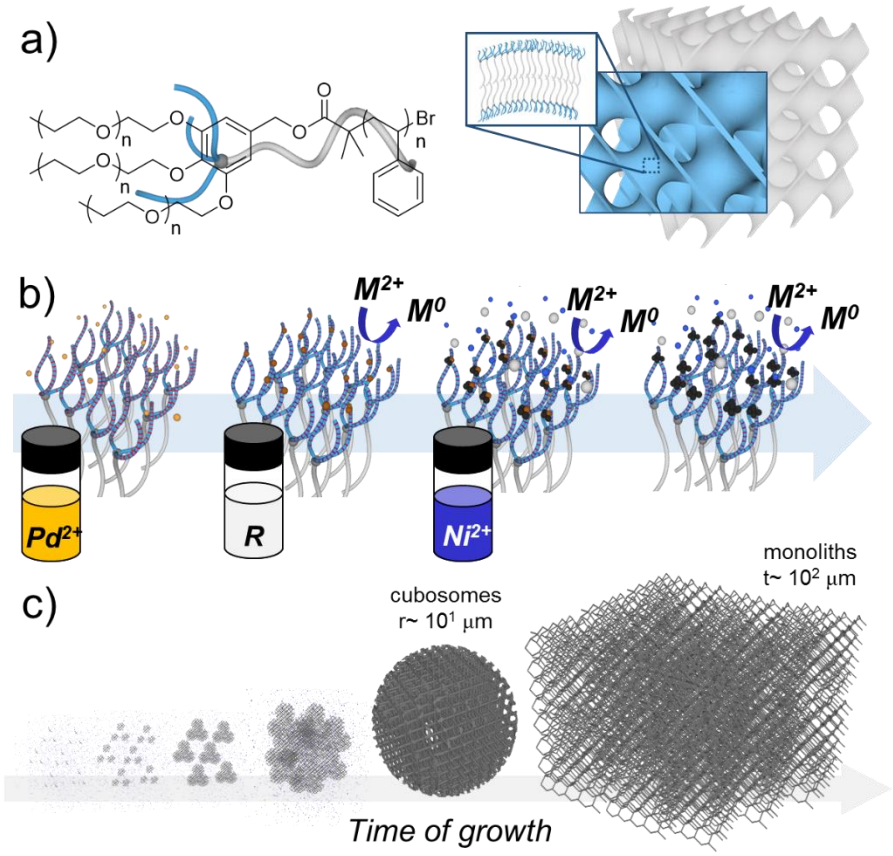

Figure 8. Templated synthesis of mesoporous 3D cubic metal architectures from the self-assembly of block copolymers. a) Bicontinuous inverse cubic mesophases are prepared from the self-assembly of branched-linear $(PEG)_3$-*b*-PS_n BCPs in a dilute solution or by SDEMS.[27–30] b) A simple two-step procedure for template activation and metal growth by *in situ* chemical reduction allows templated synthesis of mesoporous nickel architectures at ambient conditions. c) Depending on the time of growth, cubic metal mesostructures are obtained in different sizes after removing the polymer template with an organic solvent.

CHAPTER 2: RESULTS AND DISCUSSIONS

2.1 Synthesis of branched-linear $(PEG)_3$-*b*-PS_n BCPs

Synthesis of branched-linear poly(ethylene glycol)$_3$-*b*-poly(styrene)$_n$ were conducted according to precedent research.[27–30] Polymers with similar block ratio of PEG and PS were prepared to yield bicontinuous inverse cubic structures through self-assembly. According to the precedent research,[29] polymers with greater molecular weights yield bicontinuous inverse cubic structures with greater lattice constants. Therefore, three polymer molecules with different molecular weights were prepared (**Table 1**). The reaction scheme and polymer growth are shown in **Figure 9**. First, a PEG-linked macroinitiator was synthesized by tethering three PEG chains to a 3,4,5-trihydroxybenzyl ester core. Using the PEG-linked macroinitiator, polymers with three different molecular weights were prepared by atomic transfer radical polymerization (ATRP). Polymer growth was monitored by gel permeation chromatography (GPC) at different time points. Linearity of the polymer growth over reaction time and low dispersity ($D < 1.2$) marks that the polymerization followed the mechanisms of ATRP. Pure polymer was isolated and characterized with proton nuclear magnetic resonance (^{1}H NMR). A detailed synthesis procedure and structural analysis is available in the supporting information (See Appendix A).

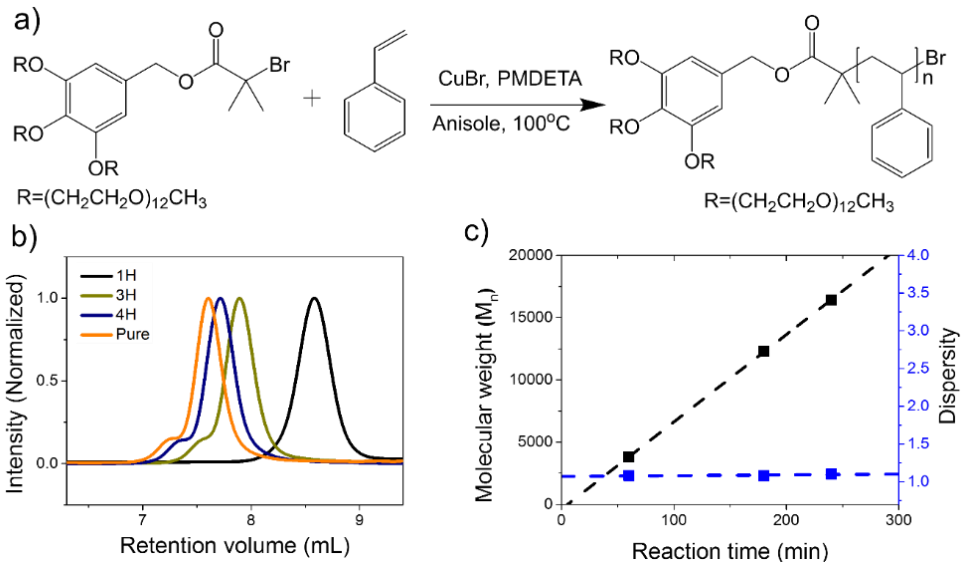

Figure 9. Synthesis of $(PEG)_3$-*b*-PS_n BCPs for template preparation. a) Reaction scheme for synthesizing $(PEG550)_3$-*b*-PS_n by ATRP. b) GPC chromatogram of the growing polymer sampled at 1, 2, and 4 hour time points and a purified product. c) Molecular weights and dispersity of the growing polymer at corresponding time points.

Table 1. List of $(PEG)_3$-*b*-PS_n BCPs synthesized by ATRP.

Polymer	M_n[a] [g/mol]	PDI[a] (M_w/M_n)	$DP_n(PS)$[b]	Block ratio[c] (f_{PEG}, %)
$(PEG550)_3$-*b*-PS_{155}	17,200	1.09	155	10.2
$(PEG750)_3$-*b*-PS_{240}	34,900	1.09	240	9.04
$(PEG1000)_3$-*b*-PS_{304}	77,400	1.13	304	9.34

[a]The number average molecular weight and molecular weight distribution was determined by GPC (THF, 35°C, 1 mL min^{-1} flow rate) calibrated with PS standards. [b] The number average degree of polymerization of PS block was determined by ^1H NMR integration. [c] The molecular weight ratio of the PEG domain to that of the PS block ($M_n(PEG550_3)$ = 1,650 g/mol; $M_n(PEG750_3)$ = 2,250 g/mol; $M_n(PEG1000_3)$ = 2,950 g/mol).

2.2 Self-assembly of $(PEG)_3$-*b*-PS_n BCPs

From our group's precedent research, [27–29] polymer molecules self-assemble into bicontinuous inverse cubic phases by solution self-assembly (**Figure 10**) and SDEMS (**Figure 11**). Depending on the method of self-assembly, spherical colloids (cubosomes) or a monolith with a cubic nanostructure can be obtained.

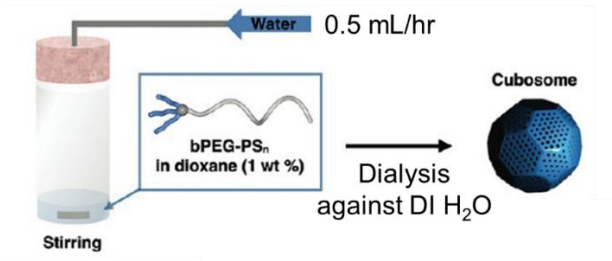

Figure 10. Schematic diagram showing solution self-assembly (cosolvent method) used to prepare colloidal polymer template. A dilute polymer solution in dioxane was stirred with a magnetic stirring bar, to which equal volume of deionized water was slowly added to yield 1:1 v/v dioxane/water emulsion of colloidal particles with a cubic nanostructure (polymer cubosomes).[28]

Polymer cubosomes were prepared by solution self-assembly by co-solvent method (**figure 10**).[27–29] First, a polymer solution (0.5-1.0 wt%) was prepared by dissolving the polymer in 1,4-dioxane in a 20 mL screw cap vial. The polymer solution was stirred with a magnetic stirring bar for at least 15 minutes to ensure homogeneity. Then, deionized water was slowly added into the polymer solution by using a programmable syringe pump. After 4 hours, the resulting emulsion was dialyzed against an excess amount of deionized water over 24 hours using a dialysis bag (molecular weight cutoff = 12–13 kDa, SpectraPor) to allow slow removal of the

organic solvent. The dialysis medium was refreshed every 4-5 hours. Finally, cubosomes were isolated by centrifugation at 14,000 g for 6 minutes.

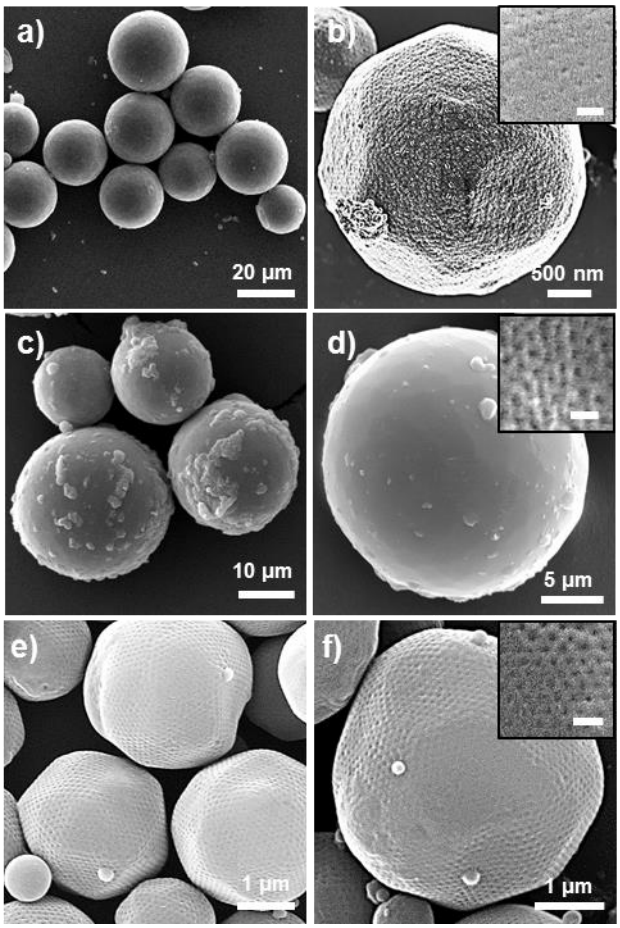

Figure 11. SEM images of colloidal polymer templates prepared by solution self-assembly by cosolvent method. a, b) $(PEG550)_3$-*b*-PS_{155} polymer cubosomes. c, d) $(PEG750)_3$-*b*-PS_{240} polymer cubosomes. e, f) $(PEG1000)_3$-*b*-PS_{304} polymer cubosomes. Inset images show periodic array of pores on the surface. Scale bar=100 nm.

Figure 11 shows the SEM images of colloidal polymer templates prepared by solution self-assembly of branched-linear $(PEG)_3$-*b*-PS_n. The inset images show the periodic array of pores on the surface. It is known in literature that only one of the two internalized channels is open to the surface.[29] Therefore, templated synthesis based on these colloidal polymer cubosomes will enable synthesis of 3D metal networks that has a lattice constant of the pore-to-pore distance of the polymer cubosomes. Image analysis of the high-resolution SEM images of the $(PEG550)_3$-*b*-PS_{155} cubosomes indicates an average pore-to-pore distance of 49.5 nm (**Figure 11b**). Image analysis of the $(PEG750)_3$-*b*-PS_{240} cubosomes indicates an average pore-to-pore distance of 57.1 nm (**Figure 11d**). Image analysis of $(PEG1000)_3$-*b*-PS_{304} cubosomes indicates an average pore-to-pore distance of 105 nm (**Figure 11f**).

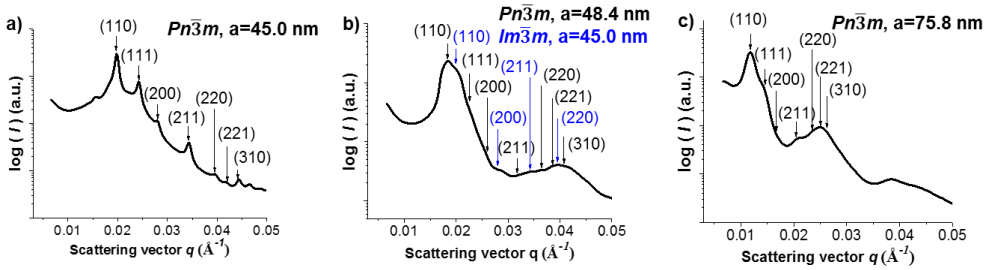

Figure 12. SAXS analysis of colloidal polymer templates. a) $(PEG550)_3$-*b*-PS_{155} polymer cubosomes (*Pn3m*, *a* = 45.0 nm); b) $(PEG750)_3$-*b*-PS_{240} polymer cubosomes (Mixture of *Pn3m*, *a* = 48.4 nm, and *Im3m*, *a* = 45.0 nm); c) $(PEG1000)_3$-*b*-PS_{304} polymer cubosomes (*Pn3m*, *a* = 75.8 nm).

The lattice symmetry and the corresponding lattice constant of the polymer cubosomes were assigned by SAXS measurements (**Figure 12**). The SAXS data of the $(PEG550)_3$-*b*-PS_{155} cubosomes in **Figure 12a** reveals that the lattice symmetry is assigned as double diamond with space group $Pn\bar{3}m$ (Schwarz D), and the

corresponding lattice constant is 45.0 nm. The SAXS data of the $(PEG750)_3$-*b*-PS_{240} cubosomes in **Figure 12b** reveals that the lattice symmetry is a mixture of double diamond (space group $Pn\bar{3}m$, Schwarz D) and primitive cubic (space group $Im\bar{3}m$, Schwarz P) with lattice constant of 48.4 nm and 45.0 nm. Combining with the SEM images, the majority of the lattice structures seems to be double diamond, as confirmed by the mesoporous 3D nickel structures synthesized therefrom. The SAXS data of the $(PEG1000)_3$-*b*-PS_{304} cubosomes in **Figure 12c** reveals that the lattice symmetry is assigned as double diamond with space group $Pn\bar{3}m$ (Schwarz D), and the corresponding lattice constant is 75.8 nm. These values confirm that self-assembly of polymer molecules with same PEG to PS block ratio but bigger molecular weights yield bicontinuous inverse cubic mesophases with greater lattice constants. It is worth mentioning that the difference in the lattice parameters of the two polymers having a PEG chain of 550 g/mol (12 repeating units) and 750 g/mol (17 repeating units) is less compared to the difference between the two polymers and the longest polymer molecule having a PEG chain of 1,000 g/mol (22 repeating units). This could be explained based on the geometry of packed chains that compose the bilayer structures. There can be more weight to the volumetric occupancy of the chains when the polymer chains are longer.

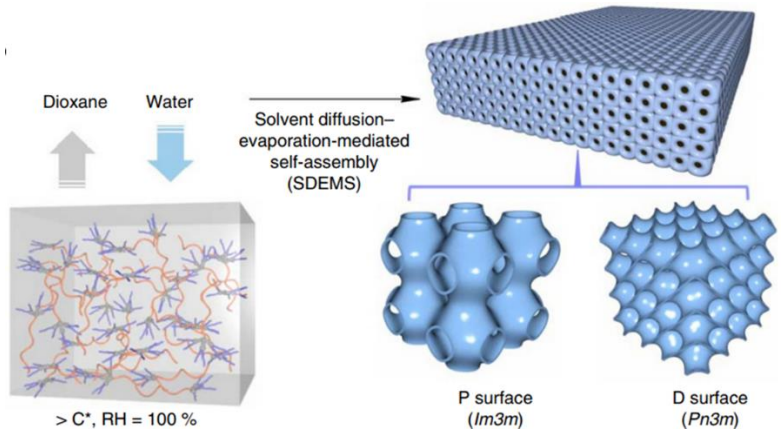

Figure 13. Schematic diagram showing solvent diffusion-evaporation mediated self-assembly (SDEMS) used to prepare monolithic polymer template. A polymer solution in dioxane was conditioned in a sealed humidity chamber (100% relative humidity, RT).[30]

Cubic monoliths were prepared by solvent diffusion-evaporation mediated self-assembly (SDEMS, **Figure 13**).[30] First, a polymer solution (12.0–13.0 wt%) was prepared by dissolving the polymer in 1,4-dioxane. The polymer solution was stirred and shaken for at least two hours to ensure homogeneity. Meanwhile, a 100% relative humidity (RH) chamber was prepared by placing 20 mL of 50% volumetric mixture of 1,4-dioxane and deionized water in a screw cap glass chamber. A 20 mL screw vial was placed inside of the chamber as a foundation, where two clean glass plates cut into the size of 0.6 cm by 0.6 cm were fixed onto. 10–20 µL of the polymer solution was carefully placed onto the glass plates. After 2–4 hours, the glass plates were removed from the chamber and were placed in deionized water for the dialysis. Deionized water was refreshed once in few hours for two days to ensure removal of

the organic solvent. The resulting monoliths were isolated and dried under atmospheric pressure at room temperature.

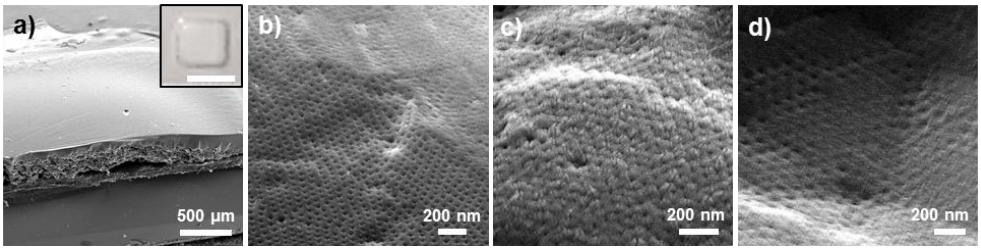

Figure 14. SEM images of monolithic polymer templates prepared by SDEMS. a, b) $(PEG550)_3$-*b*-PS_{155} cubic monolith. Inset shows a photograph of the dried polymer monolith. Scale bar = 5 mm. c) $(PEG750)_3$-*b*-PS_{240} cubic monolith. d) $(PEG1000)_3$-*b*-PS_{304} cubic monolith.

Figure 14 shows the SEM images of monolithic polymer templates prepared by SDEMS of branched-linear $(PEG)_3$-*b*-PS_nImage analysis of the high-resolution SEM images of the $(PEG550)_3$-*b*-PS_{155} monolith indicates an average pore-to-pore distance of 50.8 nm (**Figure 14b**). Image analysis of the $(PEG750)_3$-*b*-PS_{240} monolith indicates an average pore-to-pore distance of 56.1 nm (**Figure 14c**). Image analysis of $(PEG1000)_3$-*b*-PS_{304} cubosomes indicates an average pore-to-pore distance of 61.3 nm (**Figure 14d**). The lattice symmetry and the corresponding lattice constant of the polymer cubosomes were assigned by SAXS measurements (**Figure 15**). It is reported in literature that the surface of a large-area monoliths prepared by SDEMS may have some disorder on the surface (*i.e.* resulting in the presence of disordered single continuous phases) due to some residual solvent that plasticizes the PS blocks, exerting a local pressure that shifts the *Pn3m* symmetries.[30] This explains the reason

why the peaks are more diffuse than the peaks observed for the polymer cubosomes, and why there is a weak peak at low *q* region in **Figure 15a** and **15b**.

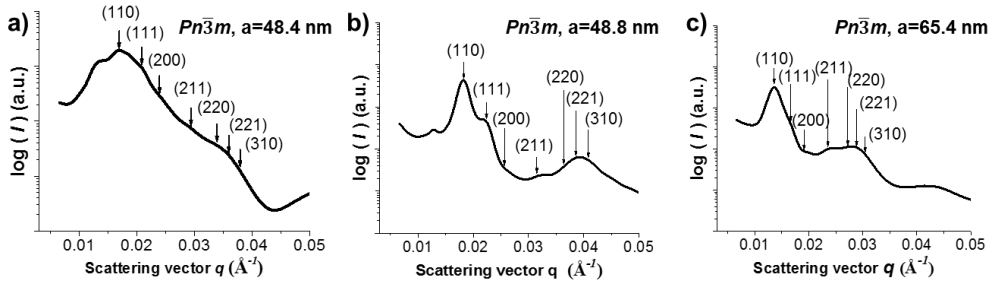

Figure 15. SAXS analysis of monolithic polymer templates. a) $(PEG550)_3$-*b*-PS_{155} cubic monolith (*Pn3m*, *a* = 48.4 nm); b) $(PEG750)_3$-*b*-PS_{240} cubic monolith (*Pn3m*, *a* = 48.8 nm); c) $(PEG1000)_3$-*b*-PS_{304} cubic monolith (*Pn3m*, *a* = 65.4 nm).

The SAXS data of the $(PEG550)_3$-*b*-PS_{155} cubic monolith in **Figure 15a** reveals that the lattice symmetry is assigned as double diamond with space group $Pn\bar{3}m$ (Schwarz D), and the corresponding lattice constant is 48.4 nm. The SAXS data of the $(PEG750)_3$-*b*-PS_{240} cubic monolith in **Figure 15b** reveals that the lattice symmetry is assigned as double diamond with space group $Pn\bar{3}m$ (Schwarz D), and the corresponding lattice constant is 48.8 nm. The SAXS data of the $(PEG1000)_3$-*b*-PS_{304} cubic monolith in **Figure 15c** reals that the lattice symmetry is assigned as double diamond with space group $Pn\bar{3}m$ (Schwarz D), and the corresponding lattice constant is 65.4 nm. In parallel to the trends in the size of lattice constants observed for polymer cubosomes, the difference in the lattice parameters of the two polymers having a PEG chain of 550 g/mol (12 repeating units) and 750 g/mol (17 repeating units) is less compared to the difference between the two polymers and the longest polymer molecule having a PEG chain of 1,000 g/mol (22 repeating units).

Since the size of the monoliths is much bigger than the polymer cubosomes, the structure is much more diverse in its distribution of crystal grains of different sizes and orientations. Also, the monoliths have more defects compared to the cubosomes as mentioned earlier.[30] This is the reason why there is a gap in the lattice parameters of polymer cubosomes and cubic monoliths prepared from the same polymer molecule.

2.3 Templated synthesis of mesoporous cubic nickel particles

A two-step nickel plating procedure was adopted from the literature[43,46] with a slight modification. Since the electron rich oxygen atoms on the surface of the template only weakly coordinate to the divalent palladium ions, the concentration of the palladium ions in the solution was optimized to achieve high density of the growing sites to cover the length scale of the template. **Table 2** summarizes the conditions of the divalent palladium solutions prepared at different concentrations.

Table 2. Conditions of divalent palladium solutions for optimizing the concentration of palladium ions for the activation of BCP templates.

	1	**2**	**3**	**4**	**5**	**6**	**7**	**8**
$PdCl_2$ [mg]	21	30	36	40	30	40	60	80
n [mmol]	0.12	0.17	0.20	0.23	0.17	0.23	0.34	0.45
V_{MeOH} [mL]	45	45	45	45	19	19	19	19
V_{HCl} [mL]	5.00	5.00	5.00	5.00	1.00	1.00	1.00	1.00
Conc. [wt%]	**0.041**	**0.061**	**0.073**	**0.080**	**0.150**	**0.200**	**0.300**	**0.400**

In order to increase the number of growing sites, methanolic solutions of 80 mg mL^{-1} to 4,000 mg mL^{-1} $PdCl_2$ were prepared. A polymer template was immersed in different conditions while keeping the reduction and nickel growth conditions the same (33mM Ni^{2+}, molar ratio of Ni and hydrazine = 12). Samples were grown for two days, isolated, and were analyzed under SEM (**Figure 16**). With same conditions, the templates were allowed to grow for 5 days (**Figure 17**).

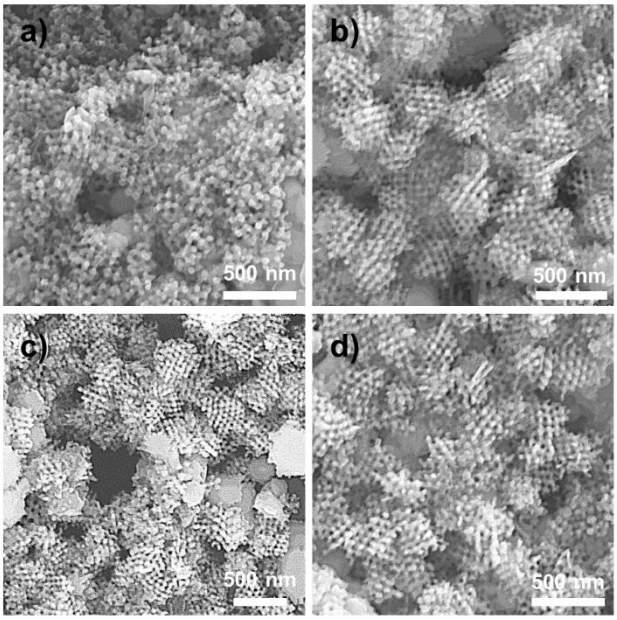

Figure 16. SEM images of nickel networks activated with different Pd^{2+} concentrations after growth in an identical Ni plating solution (33mM Ni^{2+}, molar ratio of Ni and hydrazine=12) for 2 days. a) 496 mg mL^{-1} Pd^{2+}. Domain size is 283 nm; b) 606 mg mL^{-1} Pd^{2+}. Domain size is 340 nm; c) 726 mg mL^{-1} Pd^{2+}. Domain size is 380 nm; d) 800 mg mL^{-1} Pd^{2+}. Domain size is 320 nm.

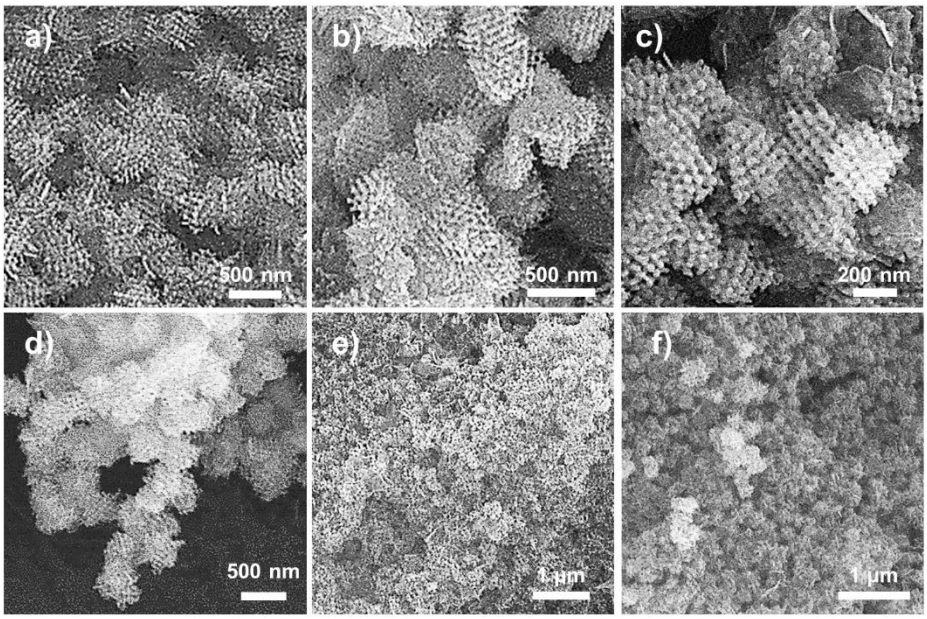

Figure 17. SEM images of nickel networks obtained at different Pd^{2+} concentrations after growth in an identical Ni plating solution (33mM Ni^{2+}, molar ratio of Ni and hydrazine=12) for 5 days. a) 606 mg mL^{-1} Pd^{2+}. Domain size is 450 nm; b) 800 mg mL^{-1} Pd^{2+}. Domain size is 478 nm; c) 1,500 mg mL^{-1} Pd^{2+}. Domain size is 340 nm; d) 2,000 mg mL^{-1} Pd^{2+}. Domain size is 434 nm; e) 3,000 mg mL^{-1} Pd^{2+}. f) 4,000 mg mL^{-1} Pd^{2+}.

Increasing the concentration of palladium precursors from 800 mg mL^{-1} to 4,000 mg mL^{-1} increased the density of growing sites and greater yield, but the overall size of the nickel obtained stopped growing at about 300 nanometers in size. Higher concentration of palladium ions increases the number of growing centers to coalesce together, thereby increasing the overall size of the products. Also, the dissolution of Pd^{2+} in methanol becomes problematic at higher concentrations. Therefore, 4,000 mg mL^{-1} Pd^{2+} solution was used for further synthesis.

Also, the molar ratio of the reductant to the divalent nickel precursors in the nickel plating solution was adjusted to increase the efficiency of the synthesis over a greater length scale. The nickel ions should be able to reach the growing fronts in throughout the entire template without being reduced to atomic nickel. The Pourbaix diagram provides thermodynamic transition metal species present in a specific condition (*e.g.* electrochemical potential, pH, temperature, etc.), and adjusting the molar ratio of the reductant to the divalent nickel ion is one way to control the rate of growth. Therefore, nickel plating solutions with different molar ratio of the reductant to Ni^{2+} were prepared (**Table 3**). Polymer templates were placed in different nickel plating solutions and were grown for five days while keeping the other conditions the same (33 mM Ni^{2+}).

Table 3. Different conditions of nickel solutions for optimizing the molar ratio of reductant to nickel ions for the growth of mesoporous nickel. R=hydrazine.

	9			**10**	**11**			**12**
$NiCl_2$ [g]	0.3636	0.2182	0.1364	0.1093	0.1093	0.1093	0.1093	0.1093
n [mmol]	2.81	1.68	1.05	0.843	0.843	0.843	0.843	0.843
V_R [mL]	0.492	0.492	0.492	0.492	0.738	0.984	1.480	1.970
V_{NH3} [mL]	3.5	3.5	3.5	3.5	3.5	3.5	3.5	3.5
V_{MeOH} [mL]	2.0	2.0	2.0	2.0	2.0	2.0	2.0	2.0
V_{water} [mL]	20.0	20.0	20.0	20.0	20.0	20.0	20.0	20.0
[R] /[Ni^{II}]	**3.6**	**6.0**	**9.6**	**12**	**18**	**24**	**36**	**48**

Figure 18 shows the SEM images of the cross-section of Ni@polymer samples grown in conditions 11 and 12. The cross section images of the intentionally broken monoliths show spherical white particles that are spread throughout the polymer template matrix (dark). It is worth noting that the spherical and spreadout mesostructured Ni particles here also confirm that the growth mechanism is the two step activation and growth from selective sites.

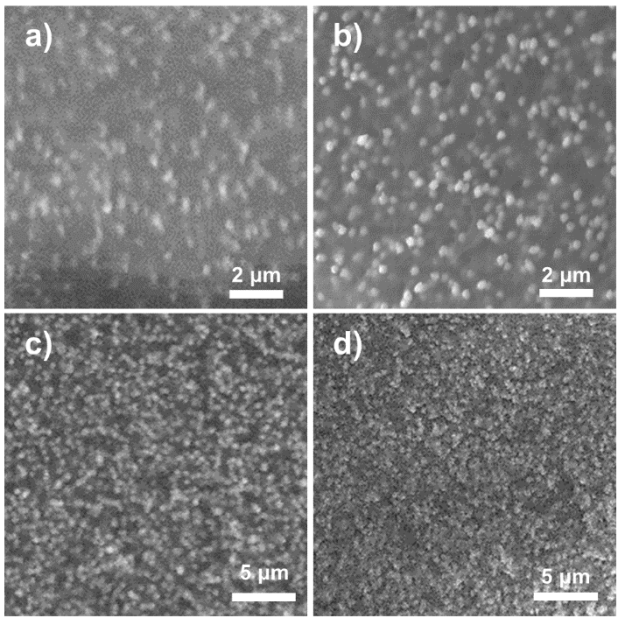

Figure 18. SEM images of the cross-section of the growing Ni@monolith in Ni plating solutions of 33 mM Ni^{2+} and different conditions. a) 1,500 mg mL^{-1} Pd^{2+}, molar ratio of Ni and hydrazine=18. b) 3,000 mg mL^{-1} Pd^{2+}, molar ratio of Ni and hydrazine=18. c) 2,000 mg mL^{-1} Pd^{2+}, molar ratio of Ni and hydrazine=48. d) 4,000 mg mL^{-1} Pd^{2+}, molar ratio of Ni and hydrazine=48.

There was no significant differences between the products synthesized with conditions 9 and 10. Therefore, condition 9 was used for further synthesis. Also, increasing the Pd(II) concentration did not show significant differences in the size and number of the growing nickel particles, as discussed in the previous section.

After conditioning the polymer cubosomes in 4,000 mg mL^{-1} Pd^{2+} solution, subsequent in-situ reduction of palladium ions with hydrazine yielded Pd-activated polymer surface for the growth of nickel (cubosome@Pd). The structure remained intact under the reductive environment. After immersing the activated cubosomes in an aqueous nickel plating solution (33 mM Ni^{2+}, R/Ni=3.6) for a week, nickel and cubosome hybrids were obtained (cubosome@Ni). After removing the polymer template with an organic solvent (THF or MC), mesoporous cubic nickel particles were obtained.

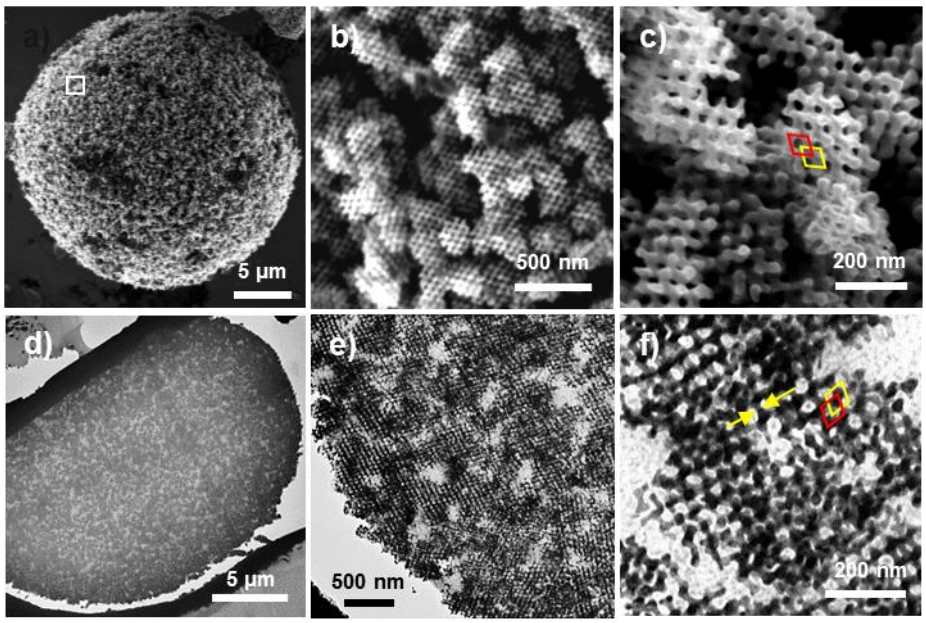

Figure 19. Electron microscopy images of the mesoporous cubic nickel particles synthesized from $(PEG550)_3$-*b*-PS_{155} polymer cubosomes. a, b, c) high-resolution FESEM images. d, e, f) TEM images of the thin sectioned mesoporous cubic nickel particles. Lattice symmetry: single diamond (red), space group *Fd3m*, *a* = 85.2 nm. Skeletal diameter = 17.2 nm (yellow arrows).

The SEM and TEM images of the mesoporous cubic nickel particles are shown in **Figure 19**. Mesoporous spherical particles grow from the palladium (0) clusters, and the growing spherical particles coalesce as the period of growth increases. Since the surface of polymer cubosomes allows access to only one of the two internal channels, the resulting nickel cubosomes replicates the template as single channel. From the image analysis, the lattice symmetry of the mesoporous cubic nickel particles can be assigned as single diamond (marked with red) with space group *Fd3m*, and the corresponding lattice constant is 86.2 nm. A detailed procedure for the calculation of lattice parameters from electron microscope images is described Appendix B.

It is noteworthy that the outer surface of the polymer template is not replicated, though the chemical composition of the surface is not different from the internal channels. After the equilibrating the template in an aqueous divalent palladium solution, the template is rinsed thoroughly with DI water several times. During this step, the weakly coordinating Pd ions on the outer surface of the polymer cubosomes are dissociated from lone pair electrons on the oxygen atoms on the surface, which allows selective activation of the template (outer surface vs. internal channel). Also, the kinetics may play a role in the selectivity of the internal surfaces because of the greater surface area. If the template is left in the nickel solution for too long, a crust may grow to cover part of the outer surface, which is seen in **Figure 19d**.

Figure 20a shows the wide-angle x-ray spectroscopy (WAXS) spectrum of the obtained mesoporous cubic nickel particles. The peaks are assigned as (111),

(200), (220) planes with a=3.5238Å, which confirms zero valent nickel as the chemical identity of the structure (JPCDS 04-0458). **Figure 20b** shows the spectrum obtained from the energy dispersive x-ray spectroscopy (EDX). The peaks at 7.46 KeV ($K\alpha$), 8.24 KeV (K_β), and 0.86 KeV ($L\alpha$) confirms that the structures are composed of nickel. The intensity of the nickel peaks accounts for 68 wt% and 56 at%. Based on the analysis, it is clear that the surface of the synthesized structures is composed of atomic nickel. The minor peaks at 8.02 KeV (Cu K_α), 0.277 KeV (C K_α) and 0.525 KeV (O K_α) originate from the carbon-coated mesh Cu TEM grids.

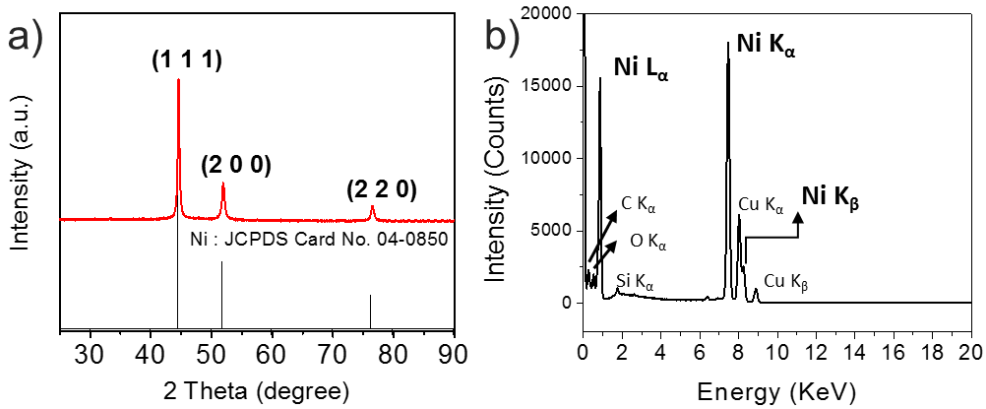

Figure 20. Characterization data for the mesoporous cubic nickel particles synthesized from $(PEG550)_3$-*b*-PS_{155} polymer cubosomes. a) WAXS spectrum showing the first three major peaks indexed as zero-valent nickel. b) EDX spectrum indicating atomic species of the sample.

Using the other two polymer templates, mesoporous cubic nickel particles with greater lattice constant and pore size was synthesized. The products obtained by using $(PEG750)_3$-*b*-PS_{240} and $(PEG1000)_3$-*b*-PS_{304} as a template were imaged with

SEM and TEM, as shown in **Figure 21 and Figure 22**. From the image analysis, the average pore-to-pore distance is 52.6 nm and 64.38 nm, respectively.

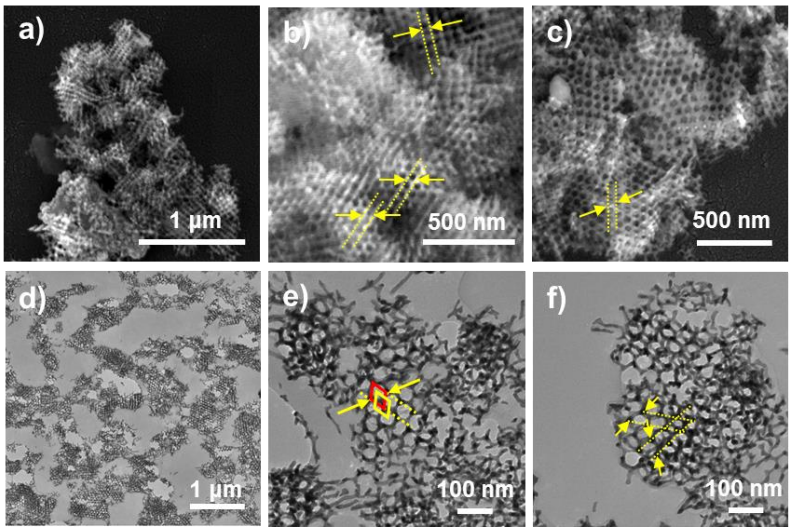

Figure 21. Electron microscopy images of the mesoporous cubic nickel synthesized from $(PEG750)_3$-*b*-PS_{240} polymer templates. a, b, c) SEM images. d, e, f) TEM images of the thin sectioned mesoporous cubic nickel particles. Lattice symmetry: single diamond, space group *Fd3m*, *a* = 74.4 nm.

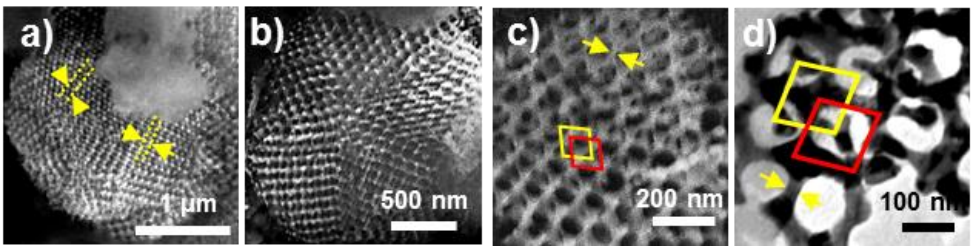

Figure 22. Electron microscopy images of the mesoporous cubic nickel synthesized from $(PEG1000)_3$-*b*-PS_{304} polymer templates. a, b, c) SEM images. d) TEM image of the thin sectioned mesoporous cubic nickel particles. Lattice symmetry: single diamond, space group *Fd3m*, *a* = 156 nm.

2.4 Templated synthesis of mesoporous cubic nickel monoliths

Activation in a palladium solution with condition 8 (4,000 mg mL^{-1} Pd^{2+}), reduction with hydrazine, and conditioning in a nickel plating solution with condition 9 (molar ratio of the R:Ni(II) = 3.6) yielded a mesoporous cubic nickel monolith that templates structure over a large volume, as shown in **Figure 23**. High resolution FESEM images show that the spherical grains are interconnected to form an intact structure. When sectioned into thin films, a lot of internal pores were observed, providing hierarchical porosity to the material.

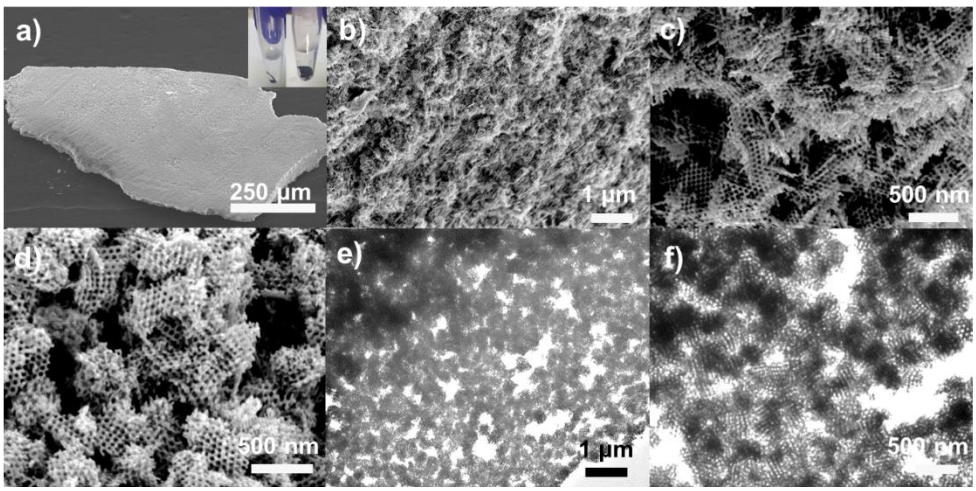

Figure 23. Electron microscope images of the mesoporous cubic nickel monolith synthesized from $(PEG550)_3$-*b*-PS_{155} polymer monoliths. (a) SEM image with (inset) an optical image; b, c, d) FESEM images; e, f) TEM images of the sectioned mesoporous Ni monolith.

The mesoporous cubic nickel monolith synthesized above did not have enough integrity under little pressure (*e.g.* holding it with a tweezer broke the edges). In order to provide denser interconnectivity of the cubic networks, concentration of the nickel

precursor in the nickel plating solutions were adjusted to achieve robust synthesis of nickel networks over a large area. Also, the nickel solution was replaced with a fresh solution every 3 days.

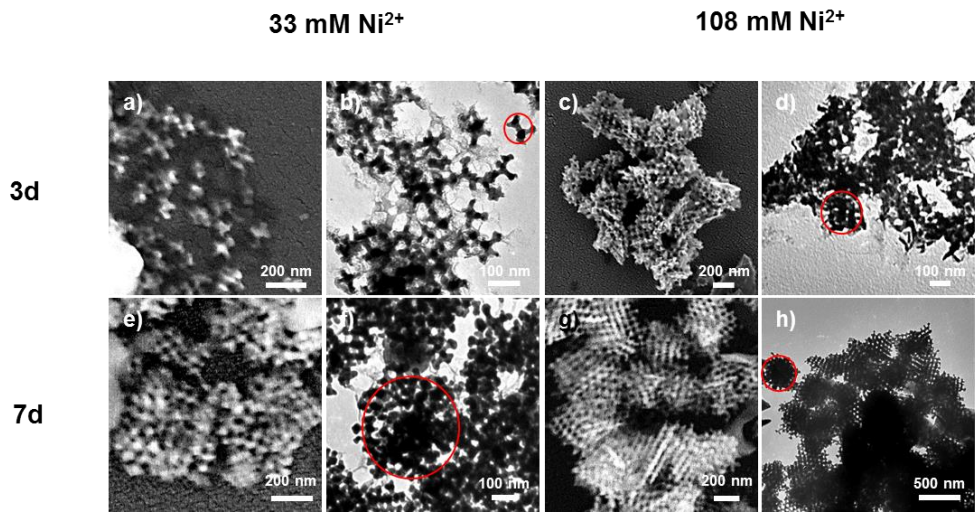

Figure 24. SEM and TEM images of the mesoporous cubic nickel networks obtained at different Ni^{2+} concentrations after activation in an identical Pd solution (22.5 mM Pd^{2+}, molar ratio of Ni and hydrazine=12) for 3 days (first row) or 7 days (second row). a, b) 33 mM Ni^{2+}. Domain size is 87.5 nm; c, d) 108 mM Ni^{2+}. Domain size is 200 nm; e, f) 33 mM Ni^{2+}. Domain size is 374 nm; g, h) 108 mM Ni^{2+}. Domain size is 403 nm.

Figure 24 shows the SEM and TEM images of the mesoporous cubic nickel networks obtained from nickel solutions of different Ni^{2+} concentrations. From comparing the products obtained from 33 mM and 108 mM Ni^{2+} conditions, higher nickel concentration brings a huge difference in the size of the obtained products. Also, when the solution was replaced with a fresh solution, further growth was observed. This is because when the plating solution is refreshed, the chemical

potential gradient (i.e. concentration difference) is reestablished between bulk solution and the solutions trapped in the internal networks of polymer templates. However, there was no significant difference in terms of templating the whole polymer monolith. In order to obtain structurally stable mesoporous cubic nickel monolith over 150 microns of thickness, the volume of the plating solution was increased to 100 mL and 200 mL.

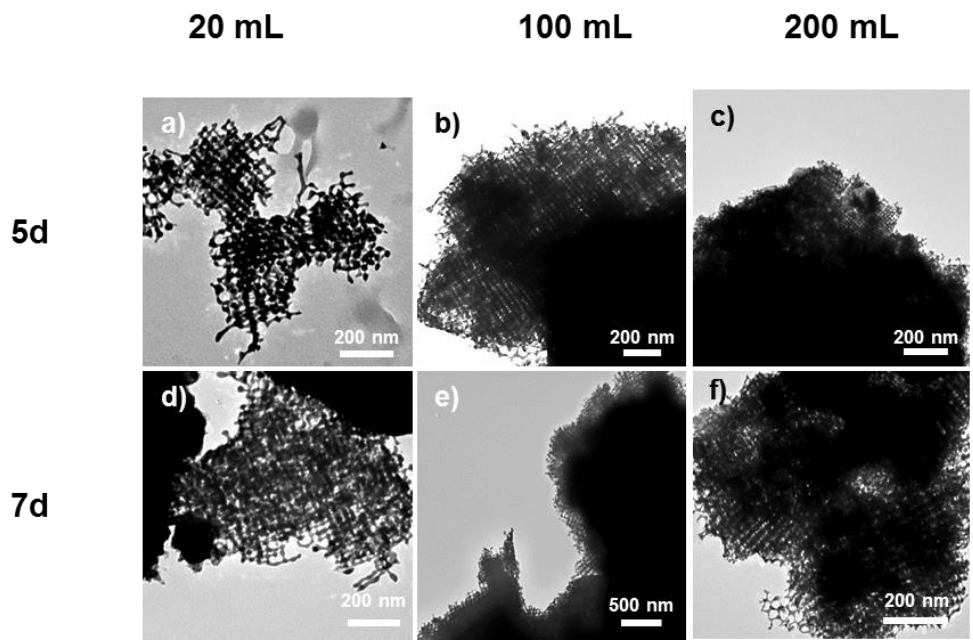

Figure 25. TEM images of the mesoporous cubic nickel networks grown in different volume of nickel plating solution for 5 days (first row) or 7 days (second row). All other conditions were the same (4,000 mg mL^{-1} Pd^{2+}, 108 mM Ni^{2+}, molar ratio of Ni and hydrazine=12).

Figure 25 shows the TEM images of the mesoporous cubic nickel networks grown in 20 mL, 100 mL, and 200 mL of nickel solutions. From comparing the products obtained from different conditions for an equal period of growth, greater

volume of the plating solution yields growth of mesoporous cubic nickel networks over a larger volume. Also, longer period of immersing the template into the nickel plating solution allowed the growth of nickel mesostructured particles to coalesce over larger volume, eventually developing a replica of the entire template. **Figure 26** shows the FESEM images of the cross section of mesoporous cubic nickel monolith synthesized with palladium activation condition (**8**) and 100 mL of the nickel plating condition (**9**). The sample was obtained after 10 days of growth.

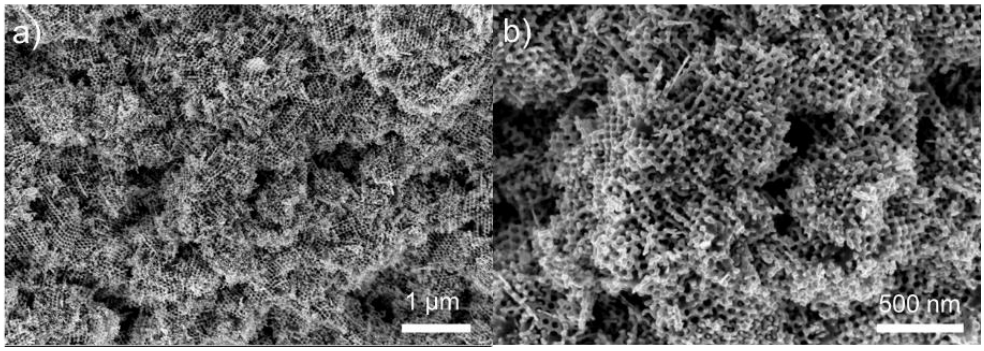

Figure 26. FESEM images of the cross section of mesoporous cubic nickel monolith synthesized in 100 mL Ni (II) plating condition (**9**) for 10 days.

After refreshing the nickel plating solution once every 3 days over two weeks, mesoporous cubic nickel monolith with thickness of >150 µm was obtained, as shown in **Figure 27**. From the image analysis, the lattice symmetry of the mesoporous cubic nickel monolith can be assigned as double diamond (marked with red) with space group *Pn3m* (**Figure 27b and Figure 27c**), and the corresponding lattice constant is 46.4 nm. A small part of the nickel monolith had lattice symmetry of double primitive cubic (**Figure 27e and figure 27f**) with space group *Im3m*, and the corresponding lattice constant is 50.0 nm.

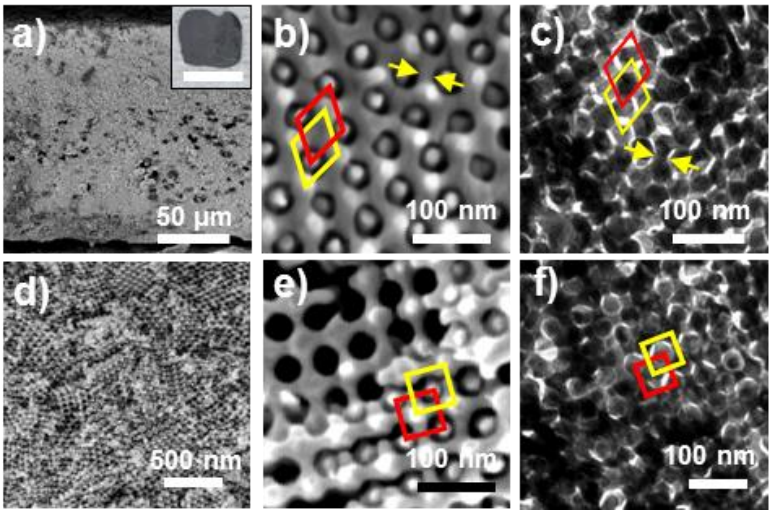

Figure 27. Electron microscopy images of the mesoporous cubic nickel monolith synthesized from $(PEG550)_3$-*b*-PS_{155} polymer monolith. a, b, d, e) High resolution FESEM images; c and f) TEM images of the mesostructured cubic nickel monolith sectioned into 100 nm thick samples. Lattice symmetry: double diamond (red and yellow) with space group *Pn3m* (a = 46.4 nm) and double primitive cubic (red and yellow) with space group *Im3m* (a = 50.0 nm). Skeletal diameter = 19.8 nm (yellow arrows). Inset image is a photograph of the mesoporous cubic nickel monolith. Scale bar=5 mm.

From the SAXS data of the $(PEG550)_3$-*b*-PS_{155} polymer monolith (**Figure 15a**), the major peaks can be assigned as *Pn3m* symmetry with lattice parameter of 48.4 nm. However, the peaks are relatively very diffuse compared to the polymer cubosomes (**Figure 12a**), and mixture of phases are possible with self-assembly over a large scale, because the structures with *Im3m* symmetry are known to have a narrow window on the phase diagram. These are the reasons that some primitive cubic lattices were observed from the SEM image analysis (**Figure 27e and Figure 27f**).

It is worth noting that to obtain a mesostructured nickel monolith with greater size, one needs to prepare the polymer template in a larger scale, scale up and repeat this simple two step procedure.

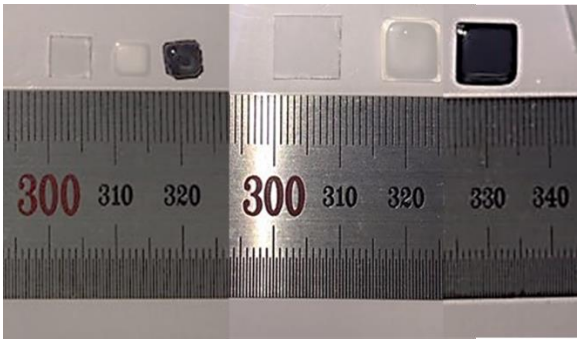

Figure 28. Photographs of a glass substrate used to prepare polymer monoliths, the prepared polymer monoliths, and the resulting Ni@polymer synthesized from the BCP template. (left) Based on a 0.6 cm X 0.6 cm glass plate. (right) Based on a 1.0 cm X 1.0 cm glass plate.

2.5 Templated synthesis of mesoporous platinum and gold

A two-step procedure was adopted from the literature[43,44] for plating platinum and gold. The mesoporous cubic platinum particles were imaged with electron microscopes, as shown in **Figures 29 and 30**. From the image analysis, the lattice symmetry of mesoporous cubic platinum particles is assigned as single diamond (red) with space group *Fd3m*, and the corresponding lattice constant is 47.7 nm. The lattice symmetry of mesoporous cubic gold particles is assigned as single primitive cubic (red) with space group *Pm3m*, and the corresponding lattice constant is 42.9 nm.

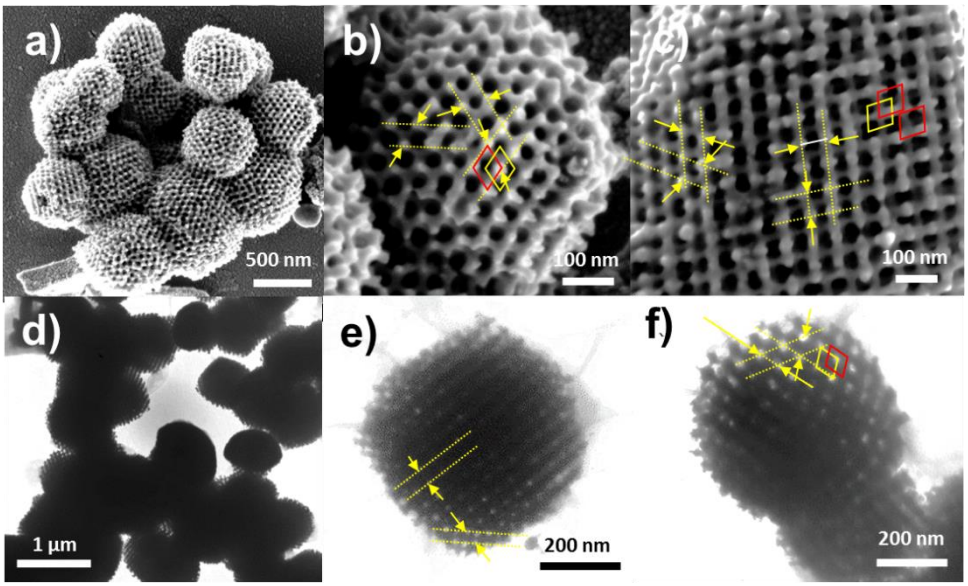

Figure 29. Electron microscopy images of the mesoporous cubic platinum particles synthesized from $(PEG550)_3$-*b*-PS_{155} polymer templates. a–c) High-resolution FESEM images; d–f) TEM images. Lattice symmetry: single diamond (red), space group *Fd3m*, *a* = 47.7 nm.

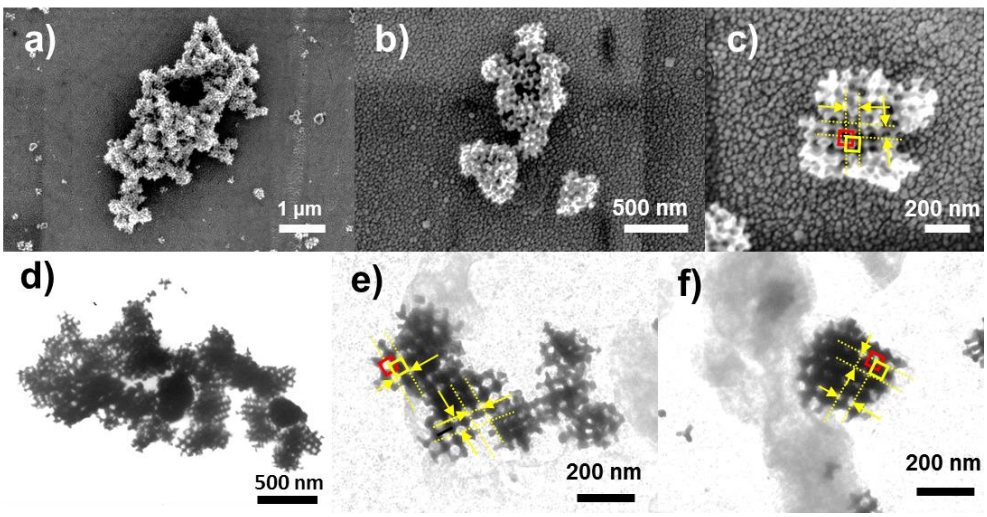

Figure 30. Electron microscopy images of the mesoporous cubic gold particles synthesized from $(PEG550)_3$-*b*-PS_{155} polymer templates. a–c) High-resolution FESEM images; d–f) TEM images. Lattice symmetry: single primitive cubic (red), space group *Pm3m*, *a* = 42.9 nm.

Figure 31 shows the WAXS data for the obtained samples. In **Figure 31a**, the peaks are assigned as (111), (200), (220), (311) planes with a=3.916 Å, which confirms zero valent platinum as the chemical identity of the structure (JCPDS 01-1194). In **Figure 31b**, the peaks are assigned as (111), (200), (220), (311), and (222) planes with a=4.079 Å, which confirms zero valent gold as the chemical identity of the structure (JCPDS 04-0784).

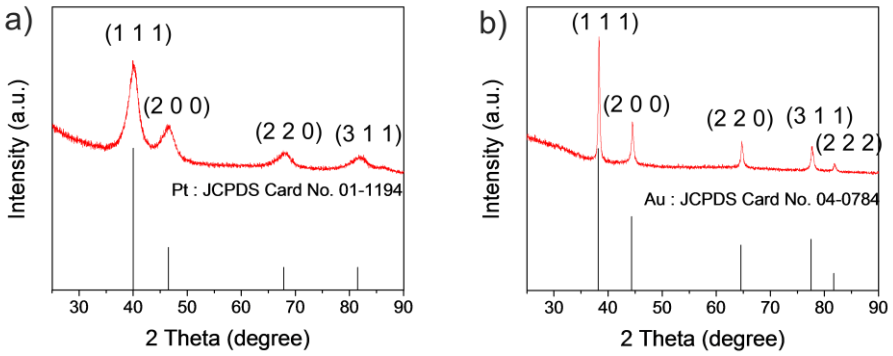

Figure 31. WAXS spectrum data for the mesoporous cubic platinum and gold particles synthesized from $(PEG550)_3$-*b*-PS_{155}. a) The peaks are indexed as zero valent platinum. b) The peaks are indexed as zero valent gold.

CHAPTER 3: CONCLUSIONS

The mesoporous 3D cubic transition metal particles or monoliths that resemble Schwarz P and D surface were synthesized by a simple and mild two-step *in situ* activation and growth of metal ions by templated synthesis of bicontinuous inverse cubic mesophases of branched-linear $(PEG)_3$-*b*-PS_n. The mesopores and interconnectivity of the uniform 3D nickel channels are expected to enhance efficient mass transport, higher specific activity, and stability. The equivalent analog made of platinum adds to the library of platinum catalysts having unique structures. The difference of these unique structures will be more pronounced in their plasmon absorbance behavior, compared to the famous gyroidal transition metal mesostructures.

This research demonstrates the synthesis of various mesoporous cubic transition metal materials without the need of calcination or electroplating, thereby making the structural transcription much easier. Especially, the mesoporous cubic nickel particles will provide a platform to synthesize new carbon allotropes when used as a template for synthesizing graphene by CVD. Since 3D cubic network structures are attracting the interests of many research scientists in the field of material chemistry, this research provides an easy access to materials having the Schwarz P and D surface, opening new opportunities for the discovery of new materials.

CHAPTER 4: EXPERIMENTAL SECTION

4.1 Materials and methods

Unless otherwise noted, all reagents and chemicals were purchased from Sigma Aldrich, Alfa Aesar, and TCI and used as received. Styrene monomer was purified by basic alumina column before use. Dichloromethane (MC) was dried over CaH_2 under N_2 and tetrahydrofuran (THF) was refluxed over a mixture of Na and benzophenone under N_2 and distilled before use. For plating baths or conditioning of the samples, deionized water was purged with N_2 before use. All reactions were performed under N_2 unless otherwise noted.

^1H NMR spectra were recorded on an Agilent 500-MR DD2 spectrometer, using $CDCl_3$ as a solvent. Molecular weights of block copolymers were measured by Agilent 1260 Infinity GPC system equipped with a PL gel 5 μm mixed D column (Agilent Technologies) and differential refractive index detectors. THF was used as an eluent with a flow rate of 1 mL min^{-1} at 30 °C and the analytical sample was filtered by using PTFE filter before injection. A PS standard (Agilent Technologies) was used for calibration.

Matrix-assisted laser desorption ionization time-of-flight mass spectroscopy (MALDI-TOF-MS) was performed on a Bruker Ultraflex III TOF-TOF mass spectrometer equipped with a nitrogen laser (335 nm). The experimental sample was obtained by mixing a THF solution of block copolymers (5 mg mL^{-1}) and the THF solution of matrix (sinapinic acid or dithranol, 10 mg mL^{-1}). The prepared mixture was loaded on the MALDI plate and dried at room temperature before measurement.

Scanning electron microscopy (SEM) was performed on Hitachi S-4300 at an acceleration voltage of 15 kV and a Zeiss Supra 55VP FESEM at an acceleration voltage of 2 kV. Dried polymer cubosomes were placed on a conductive carbon tape and then coated with Pt by using a Hitachi E-1030 ion sputter coater (20 mA, 60s).

Transmission electron microscopy (TEM) was performed on a Hitachi 7600 operating at 100 kV and a JEOL JEM-3010 operating at 300 kV. TEM Specimens were prepared by the following procedure: the samples were dispersed in MC with the aid of 3 min of ultrasonic vibration. Then a drop of the solution was transferred onto a carbon-coated Copper grid (200 mesh, EM Science), and the grids was dried overnight. The morphologies of polymer nanostructures and metal mesostructures were measured by analyzing TEM images with ImageJ software. Energy dispersive X-ray spectroscopy (EDX) was recorded to determine the composition of the obtained products.

Powder X-ray diffraction (XRD) patterns of all the products obtained in this work were recorded with a Bruker D8 Advance X-ray powder diffractometer with monochromatized Cu Kα radiation (λ = 1.5406 Å). The surface composition of the prepared samples was analyzed by X-ray photoelectron spectroscopy (XPS) using an AXIS His spectrometer (Kratos Analytic Ltd) equipped with a monochromatic Al Kα source at a power of 300 W.

4.2 Synthesis of poly(ethylene glycol)$_3$-*block*-poly(styrene) ((PEG)$_3$-*b*-PS)

(PEG)$_3$-*b*-PS was synthesized according to the method established by our group.[27–30] In brief description, a macroinitiator for growing styrene block was synthesized first by an EDC coupling of 3,4,5-polyethyleneglycolic-benzyl alcohol with alpha-bromoisobutyric bromide. The structure of the macroinitiator was confirmed by ^{1}H NMR spectroscopy and MALDI-TOF. Subsequently, the macroinitiator was mixed with styrene, CuBr, PMDETA, and anisole under N_2 purging. The mixture was degassed with N_2 and was warmed to 95^{o}C. For detailed information and characterization data, see supporting information.

4.3 Preparation of bicontinuous colloidal cubic particles (cubosomes)

The mesoporous inverse cubic particles were prepared according to the procedure established by our group.[27–30] In a brief description, 20 mg of the a pure (PEG)$_3$-*b*-PS polymer and 2 mL of 1,4-dioxane was added in a capped vial (1 wt%), and the polymer solution was stirred for 3 hours at room temperature. Water was added at a controlled rate (1 mL h^{-1}, total of 2 mL) to the solution with vigorous stirring (850 rpm). The resulting suspension was dialyzed against waster for 24 hours using dialysis bag (molecular weight cutoff = ~12-13 kDa, SpectraPor) to allow slow removal of the organic solvent.

4.4 Preparation of mesoporous cubic monoliths

The mesoporous cubic monoliths were prepared according to the procedure established by our group.[27–30] In a brief description, a pure $(PEG)_3$-*b*-PS polymer was dissolved in 1,4-dioxane (13 wt%), and was stirred for 2 hours at room temperature. The polymer solution was placed in a chamber with 50% relative humidity for 2 hours at room temperature. The resulting membranes were subsequently washed with deionized water for 2 days.

4.5 Preparation of mesoporous nickel network

The procedure was adapted from the literature[42,45] with slight modification. First, a pale orange solution containing palladium (II) chloride ($PdCl_2$, Sigma-Aldrich, 0.47 – 4.21 mg mL^{-1}) in methanol and 1N hydrogen chloride solution was prepared. Then, a mesoporous inverse cubic $(PEG)_3$-*b*-PS template was immersed in the prepared Pd^{2+} solution. After 3 hours, the polymer template was taken out from the Pd^{2+} solution and was rinsed thoroughly with water and ethanol for several times. Then, the washed template was immersed in a 50% hydrazinium hydroxide solution ($N_2H_4 \cdot H_2O$, Alfa Aesar) overnight. The template was taken out and was rinsed thoroughly with water and ethanol for several times. Then, the template was immersed in a clear blue aqueous solution containing nickel (II) chloride hexahydrate ($NiCl_2 \cdot 6H_2O$, Sigma-Aldrich, 54.65 mg mL^{-1}), hydrazinium hydroxide ($N_2H_4 \cdot H_2O$, Alfa Aesar, 196.7 mg mL^{-1}), 35% ammonia solution, and methanol to allow Pd-catalyzed nickel growth.

4.6 Preparation of mesoporous platinum network

The procedure was adapted from the literature.[44] In a brief description, the polymer template was first immersed in a pale orange aqueous solution containing hydrogen hexachloroplatinate (IV) hexahydrate ($H_2PtCl_6 \cdot 6H_2O$, Alfa Aesar, 3.5 mg mL^{-1}) in methanol. After 3 hours, the templates were taken out of the solution and thoroughly rinsed with water and ethanol several times. Then, the polymer template was immersed in a 50% hydrazinium hydroxide solution overnight. After rinsing with water and ethanol, the template was immersed in a methanolic solution containing hydrogen hexachloroplatinate (IV) hexahydrate ($H_2PtCl_6 \cdot 6H_2O$, Alfa Aesar, 2.5 mg mL^{-1}) and 1M ascorbic acid.

4.7 Preparation of mesoporous gold network

The procedure was adapted from the literature.[43] In a brief description, a polymer template was first immersed in a yellow solution containing hydrogen tetrachloroaurate (III) trihydrate ($HAuCl_4 \cdot 3H_2O$, Alfa Aesar, 3.45 mg mL^{-1}) in methanol. After 3 hours, the templates were taken out of the solution and thoroughly rinsed with water and ethanol several times. Then, the polymer template was immersed in a 50% hydrazinium hydroxide solution overnight. After rinsing with water and ethanol, the template was immersed in a solution containing hydrogen tetrachloroaurate (III) trihydrate ($HAuCl_4 \cdot 3H_2O$, Alfa Aesar, 5 mg mL^{-1}) in methanol, hydrazinium hydroxide ($N_2H_4 \cdot H_2O$, Alfa Aesar, 196.7 mg mL^{-1}), 1N hydrogen chloride solution, 35% ammonia solution, and methanol.

4.8 Preparation of mesoporous copper network

The procedure for preparing mesoporous nickel was modified and optimized to yield metallic copper. A polymer template was first immersed in a pale orange solution containing palladium (II) chloride ($PdCl_2$, Sigma-Aldrich, 0.47 – 4.21 mg mL^{-1}) in methanol and 1N hydrogen chloride. After 3 hours, the polymer template was taken out from the Pd^{2+} solution and was rinsed thoroughly with water and ethanol for several times. Then, the washed template was immersed in a 50% hydrazinium hydroxide solution ($N_2H_4 \cdot H_2O$, Alfa Aesar) overnight. The template was taken out and was rinsed thoroughly with water and ethanol for several times. Then, the template was immersed in a pale blue solution containing copper (II) sulfate pentahydrate ($CuSO_4 \cdot 5H_2O$, Alfa Aesar, 10.55 mg mL^{-1}) in water, hydrazinium hydroxide ($N_2H_4 \cdot H_2O$, Alfa Aesar, 9.50 mg mL^{-1}), 35% ammonia solution, and methanol.

REFERENCES

1. Schwarz, H. A. Gesammelte Mathematische Abhandlungen; Springer: Berlin, 1890.

2. Riemann, B. Über die Fläche vom kleinsten Inhalt bei gegebener Begrenzung. *Abhandlungen der Königlichen Gesellschaft der Wissenschaften zu Göttingen*, **1867,** *13*, 3–52.

3. Andersson, S.; Hyde, S.T.; Larsson, K.; Lidin, S. *Chemical Reviews*, **1988,** *88*, 221–242.

4. Schoen, A. H. Infinite periodic minimal surfaces without self-intersections, NASA Technical Note TN D-5541, NASA, USA **1970**.

5. Han, L.; Che, S. *Adv. Mater*. **2018,** *30*, e1705708.

6. Lidin, S.; Larsson, S. *J. Chem. Soc. Faraday Trans*, **1990,** *86*, 769–775.

7. Images by Minimal Surfaces Repository (https://minimalsurfaces.blog/) are licensed under CC BY-SA 4.0 (https://creativecommons.org/licenses/by-sa/4.0/).

8. Neovius, E. R. Bestimmung Zweier Spezieller Periodische Minimalflächen; J. C. Frenckel & Sohn: Helsinki, 1883.

9. Larsson, K.; Fontell, K.; Krogh, N. *Chem. Phys. Lipids*, **1980,** *27*, 321.

10. Saranathan, V.; Osuji, C. O.; Mochrie, S. G. J.; Noh, H.; Narayanan, S.; Sandy, A.; Dufresne, E. R.; Prum, R. O. *Proc. Natl. Acad. Sci. USA*, **2010,** *107*, 11676–11681.

11. Luzzati, V.; Tardieu, A.; Gulik-Krzywicki, T. *Nature*, **1968,** *217*, 1028–1030.

12. Qiu, H.; Caffrey, M. *Biomaterials*, **2000,** *21*, 223–234.

13. Tenchov, B.; MacDonald, R. C.; Siegel, D. P. *Biophys. J*. **2006,** *91*, 2508–2516.

14. Almgren, M., Edwards, K. & Karlsson, G. *Colloid Surf. A,* **2000,** *174,* 3–21.

15. Demurtas, D.; Guichard, P.; Martiel, I.; Mezzenga, R.; Hebert, C.; Sagalowicz, L. *Nat. Commun.* **2015,** *5,* 8915.

16. Leikin, S. L.; Kozolv, M. M.; Chernomordik, L. V.; Markin, V. S.; Chizmadzhev, Y. A. *J. Theor. Biol.* **1987,** *129,* 411–425.

17. Salentinig, S.; Phan, S.; Khan, J.; Hawley, A.; Boyd, B. J. *ACS Nano,* **2013,** *7,* 10904–10911.

18. Porter, C. J. H.; Revaskis, N. H.; Charman, W. N. *Nat. Rev*. **2007,** *6,* 231–248.

19. Zabara, A.; Negrini, R.; Onaca-Fischer, O.; Mezzenga, R. *Small,* **2013**, *9*, 3602–3621.

20. Kulkarni, C. V.; Tang, T.-Y.; Seddon, A. M.; Seddon, J. M.; Ces, O.; Templer, R. H. *Soft Matter,* **2010,** *6,* 3191–3194.

21. Conn, C. E.; Darmanin, C.; Mulet, X.; Hawley, A.; Drummond, C. J. *Soft Matter,* **2012,** *8,* 6884–6896.

22. Zeng, X.; Prehm, M.; Ungar, G.; Tschierske, C.; Liu, F. *Angew. Chem. Int. Ed.* **2016,** *55,* 8324–8327.

23. Poppe, S.; Cheng, X.; Chen, C.; Zeng, X.; Zhang, R.-B.; Liu, F.; Ungar, G.; Tschierske, C. *J. Am. Chem. Soc.* **2020,** *142,* 3296−3300.

24. Politakos, N.; Ntoukas, E.; Avgeropoulos, A.; Krikorian, V.; Pate, B. D.; Thomas, E. L.; Hill, R. M. *J. Polym. Sci., Part B: Polym. Phys.* **2009,** *47,* 2419−2427.

25. Ho, R. M.; Chiang, Y. W.; Chen, C. K.; Wang, H. W.; Hasegawa, H.; Akasaka, S.; Thomas, E. L.; Burger, C.; Hsiao, B. S. *J. Am. Chem. Soc*. **2009,** *131*, 18533–18542.

26. Epps, T. H.; Cochran, E. W.; Balley, T. S.; Waletzko, R. S.; Hardy, C. M.; Bates, F. S. *Macromolecules*, **2004,** *37*, 8325–8341.

27. La, Y.; Park, C.; Shin, T. J.; Joo, S. H.; Kang, S.; Kim, K. T. *Nat. Chem*. **2014,** *6*, 534–541.

28. An, T. H.; La, Y.; Cho, A.; Jeong, M. G.; Shin, T. J.; Park, C.; Kim, K. T. *ACS Nano*, **2015,** *9*, 3084–3096.

29. La, Y.; Song, J.; Jeong, M. G.; Cho, A.; Jin, S.-M.; Lee, E.; Kim, K. T. *Nat. Commun*. **2018,** *9*, 5327.

30. Park, C.; La, Y.; An, T. H.; Jeong, H. Y.; Kang, S.; Joo, S. H.; Ahn, H.; Shin, T. J.; Kim, K. T. *Nat. Commun*. **2015,** *6*, 6392.

31. Meuler, A. J.; Hillmyer, M. A.; Bates, F. S. *Macromolecules*, **2009,** *42*, 7221–7250.

32. Bates, F. S. *Science*, **1991,** *251*, 898–905.

33. Bates, F. S.; Fredrickson, G. H. *Annu. Rev. Phys. Chem*. **1990,** *41*, 525–557.

34. Rauber, M.; Alber, I.; Müller, S.; Neumann, R.; Picht, O.; Roth, C.; Schökel, A.; Toimil-Molares, M. EU.; Ensinger, W. *Nano Lett.* **2011,** *11*, 2304–2310.

35. Zhang, H.; Yu, X.; Braun, P.V. *Nature Nanotechnology*, **2011,** *6*, 277−281.

36. Kibsgaard, J.; Gorlin, Y.; Chen, Z.; Jaramillo, T.F. *J. Am. Chem. Soc*. **2012,** *134*, 7758−7765.

37. Crossland, E.J.W.; Kamperman, M.; Nedelcu, M.; Ducati, C.; Wiesner, U.; Smilgies, D.M.; Toombes, G.E.S.; Hillmyer, M.A.; Ludwigs, S.; Steiner, U.; Snaith, H.J. *Nano Lett.* **2009,** *9,* 2807−2812.

38. Wei, D.; Scherer, M.R.J.; Bower, C.; Andrew, P.; Ryhanen, T.; Steiner, U. *Nano Lett.* **2012,** *12,* 1857−1862.

39. Robbins, S.W.; Beaucage, P.A.; Sai, H.; Tan, K.W.; Werner, J.G.; Sethna, J.P.; DiSalvo, F.J.; Gruner, S.M.; Van Dover, R.B.; Wiesner, U. *Science Advances*, **2016,** *2,* e1501119

40. Urade, V. N.; Wei, T.-C.; Tate, M. P.; Kowalski, J. D.; Hillhouse, H. W. *Chem. Mater*. **2007,** *19,* 768–777.

41. Hashimoto, T.; Tsutsumi, K.; Funaki, Y. *Langmuir*, **1997,** *13*, 6869–6872.

42. Hsueh, H.-Y.; Huang, Y.-C.; Ho, R.-M.; Lai, C.-H.; Makida, T.; Hasegawa, H. *Adv. Mater.* **2011,** *23,* 3041–3046.

43. Hsueh, H.-Y.; Chen, H.-Y.; Hung, Y.-C.; Ling, Y.-C.; Gwo, S.; Ho, R.-M. *Adv. Mater*. **2013,** *25,* 1780–1786.

44. Cheng, C.-F.; Hsueh, H.-Y.; Lai, C.-H.; Pan, C.-J.; Hwang, B.-J.; Hu, C.-C.; Ho, R.-M. *NPG Asia Mater.* **2015,** *7,* e170.

45. Yang, K.-C.; Yao, C.-T.; Huang, L.-Y.; Tsai, J.-C.; Hung, W.-S.; Hsueh, H.-Y.; Ho, R.-M. *NPG Asia Mater.* **2019,** *11,* 9.

46. Kroto, H. W.; Heath, J. R.; O'Brien, S. C.; Curl, R. F.; Smalley, R. E. *Nature*, **1985,** *318,* 162–163.

47. Novoselov, K. S.; Geim, A. K.; Morozov, S. V.; Jiang, D.; Zhang, Y.; Dubonos, S. V.; Grigorieva, I. V.; Firsov, A. A. *Science*, **2004,** *306,* 666–669.

48. Mackay, A.L.; Terrones, H. *Nature,* **1991,** *352,* 762.

49. Lenosky, T.; Gonze, X.; Teter, M.; Elser, V. *Nature,* **1992,** *355,* 333–335.

50. Jung, G. S.; Buehler, M. J. *Nano Lett.* **2018,** *18,* 4845−4853.

51. Kim, K.; Lee, T.; Kwon, Y.; Seo, Y.; Song, J.; Park, J. K.; Lee, H.; Park, J. Y.; Ihee, H.; Cho, S. J.; Ryoo, R. *Nature,* **2016,** *535,* 131–135.

52. Braun, E.; Lee, Y.; Mohamad S. M.; Barthel, S.; Mercado, R.; Baburin, I. A.; Proserpio, D. M.; Smit, B. *PNAS,* **2018,** *115,* E8116–E8124.

53. Cebo, T.; Aria, A. I.; Dolan, J. A.; Weatherup, R. S.; Nakanishi, K.; Kidambi, P. R.; Divitini, G.; Ducati, C.; Steiner, U.; Hofmann, S. *Appl. Phys. Lett.* **2017,** *111,* 253103.

APPENDIX A: SUPPORTING INFORMATION

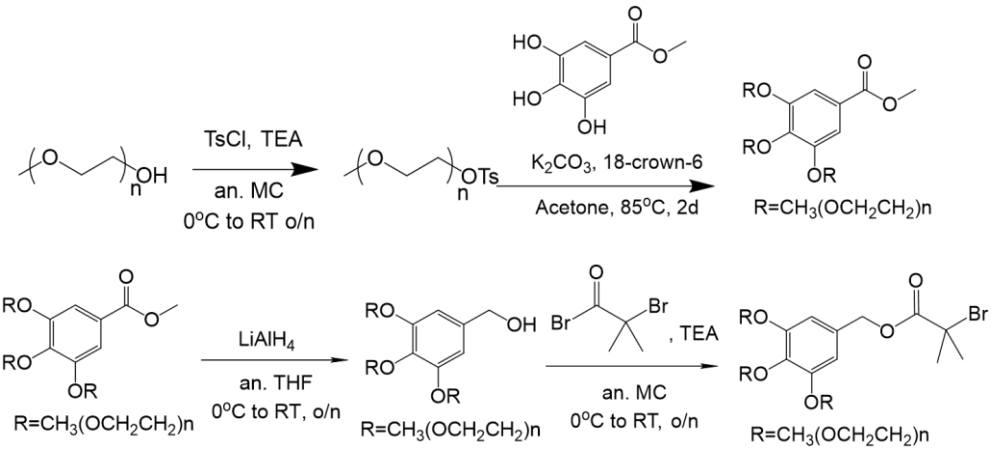

Scheme A1. Synthetic scheme for preparing α-bromoisobutyryl-3,4,5-tris(polyethylene glycol) benzyl ester Macroinitiator for the ATRP of $(PEG)_3$-*b*-PS_n BCPs.

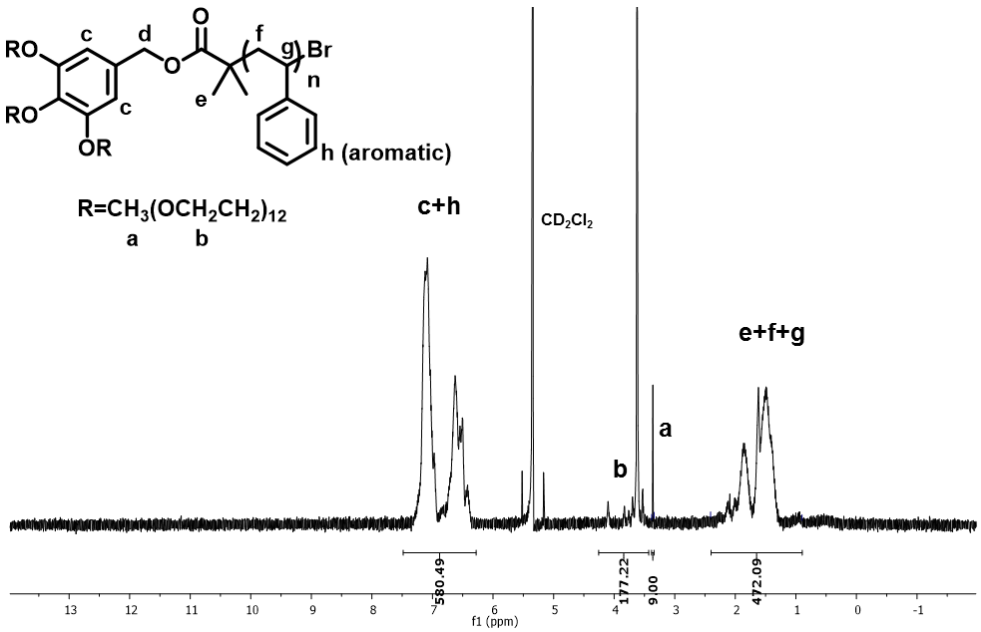

Figure A1. ^{1}H NMR spectrum of $(PEG550)_3$-*b*-PS_{155} BCP (500 MHz, CD_2Cl_2).

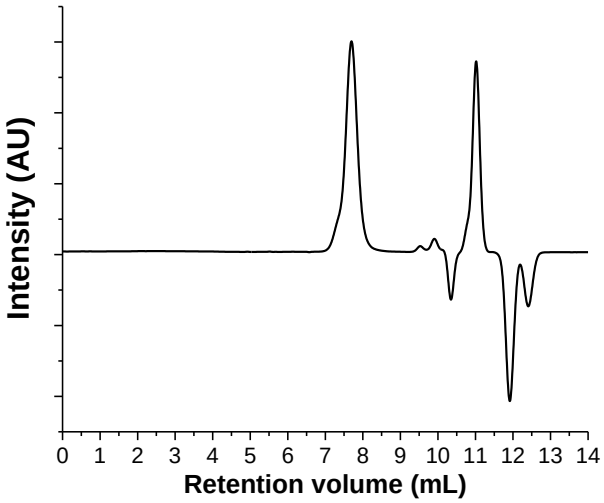

Figure A2. GPC chromatogram of $(PEG550)_3$-*b*-PS_{155} BCP (THF, 35ºC, 1 mL min^{-1} flow rate).

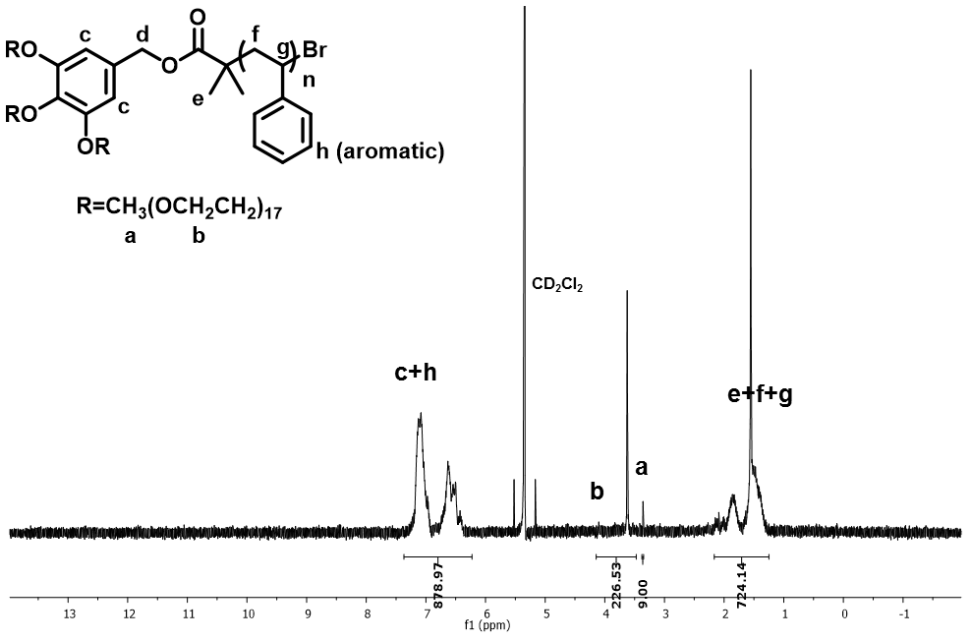

Figure A3. ^1H NMR spectrum of $(PEG750)_3$-*b*-PS_{240} BCP (500 MHz, CD_2Cl_2).

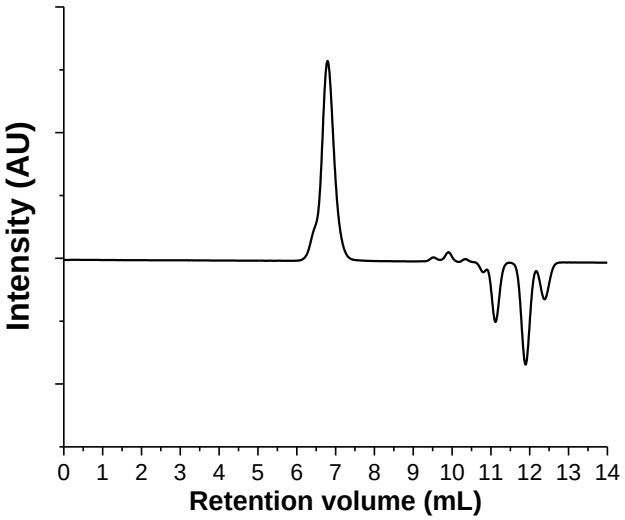

Figure A4. GPC chromatogram of $(PEG750)_3$-*b*-PS_{240} BCP (THF, 35°C, 1 mL min^{-1} flow rate).

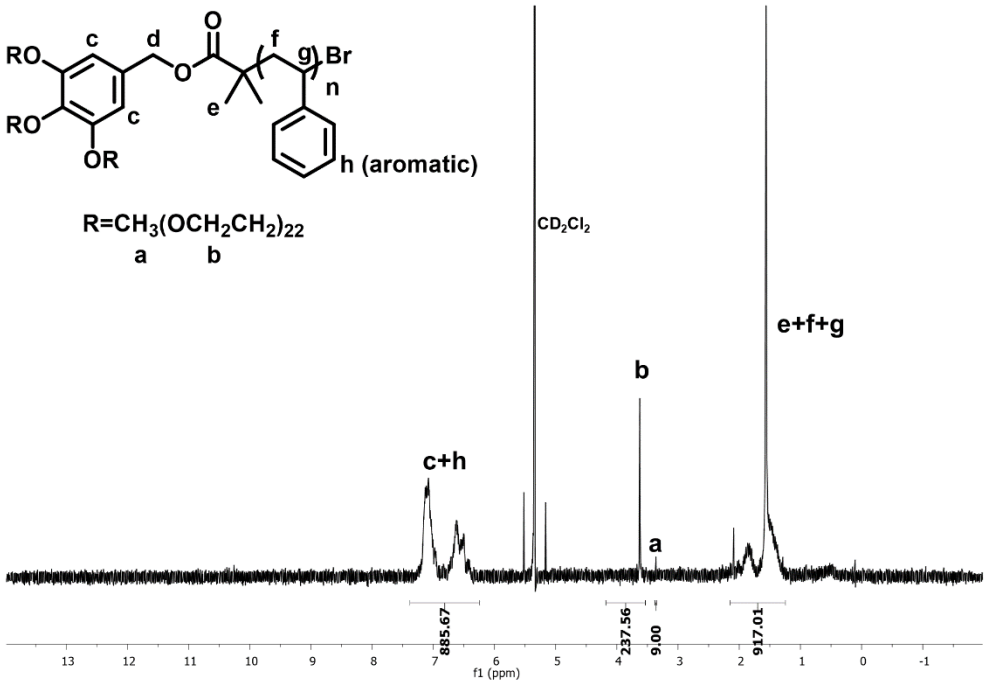

Figure A5. ^1H NMR spectrum of $(PEG1000)_3$-*b*-PS_{304} BCP (500 MHz, CD_2Cl_2).

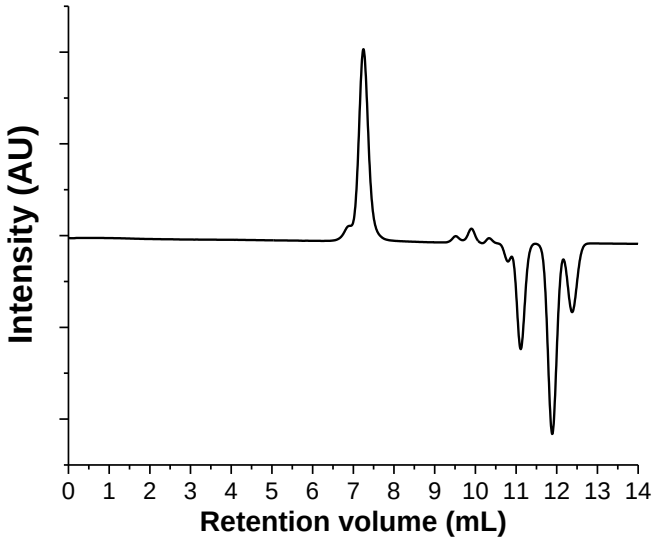

Figure A6. GPC chromatogram of $(PEG1000)_3$-*b*-PS_{304} BCP (THF, 35°C, 1 mL min^{-1} flow rate).

APPENDIX B: CALCULATION OF LATTICE PARAMETERS

From high-resolution EM images, the lattice parameters were estimated by drawing skeletal unit cells of the corresponding single (*Fd3m*) or double (*Pn3m*) diamond lattices. For the analysis of the right lattice, two rhombuses of an equal size were placed onto the EM images showing the (111) planes of *Pn3m* or *Fd3m*. First, the vertices of one rhombus was fitted to match the lattice points of the single diamond lattice. Then, the fitted rhombus was copied and the copied rhombus was shifted to match the centers of the pores (*Fd3m*) or the centers of the lattice points of the second lattice (*Pn3m*).

For *Fd3m*, the length of a side of the rhombus corresponds to the pore-to-pore distance *d*, which is equal to $\frac{\sqrt{2}}{2}\mathbf{a}$**.** From the value of *d*, lattice parameter *a* was calculated. For *Pn3m*, the length of the rhombus corresponds to the diagonal distance, which is equal to $\sqrt{2}\boldsymbol{a}$. From the value of this length, lattice parameter *a* was calculated.

국문초록

블록 공중합체의 자기조립을 통한 메조기공성 3 차원 입방체 금속재료의 주형합성

이 희 림

화학부 고분자화학 전공

서울대학교 대학원

수학 및 구조 생물학에 의해 정의되고 발견된 서로 교차하지 않는 규칙적인 최소평면은 화학자와 재료과학자들로 하여금 나노 및 메조 크기의 기공을 가지면서 연결된 채널을 규칙적으로 가지고 있는 복잡한 구조들로 자기조립을 하는 다양한 분자를 설계할 수 있도록 영향을 주었다. 주형합성법은 이러한 구조들을 다양한 고상재료로 옮길수 있게하여 더 빠른 물질 전달율, 높은 면적대비 활성도와 안정성을 가진 재료의 개발에 있어 유용한 플랫폼을 제공하였다.

종래에는 재료에 구조를 부여하고자 할 경우 자연계에 가장 흔하게 발견되는 세가지의 입방형 구조인 슈와츠 D, G, P 면 중 오직 한 가지 종류에 대한 연구가 활발하였다. 본 연구에서는 아직 비교적 활발히 연구되지 못한 다른 두가지 슈와츠 D, P 면을 이용하여 규칙적이고 서로 연결되어있으며 결정성을 가지는 메조기공성 니켈, 백금, 금 재료를 에너지 집약적인 하소나 전기 도금법을 쓰지 않고 온화한 조건에서 두 단계의 화학적 환원반응을 이용하여 합성하였다.

니켈 재료의 경우 탄소재료의 합성을 위한 화학적 기상 증착법(CVD)의 기판으로 이용되왔기 때문에 본 연구에서 합성된 메조기공성 니켈은 음수의 가우시안 곡률을 가지는 탄소 동소체의 발견에 있어 중요한 역할을 할 것으로 기대된다. 또한 니켈은 중금속 촉매를 대체할수있는 값싼 촉매재료로 개발되고 있고 백금 또한 구조를 부여하여 표면적과 활성도를 높이는 등 다방면으로 개발되고있기때문에 향후 폭넓은 활용이 가능할것으로 기대된다. 잘 알려진 자이로이드형 (슈와츠 G 면) 구조를 가진 재료들과 본 연구에서 합성된 구조들과의 차이점은 표면 플라즈몬 공명에서 두드러질것으로 기대된다. 따라서 슈와츠 P 및 D 면을 갖는 메조기공성 금 재료도 합성해보였다. 본 연구는 지금껏 자세히 연구되지 못한 슈와츠 P 및 D 면을 갖는 구조가 재료에 가져오는 독특한 특성들에 대한 연구 증진에 기여할것으로 기대된다.

……

주요어 : 주형합성, 자기조립, 친양쪽성체, 블록 공중합체, 메조기공구조, 금속 도금, 재료화학

학 번 : 2017-26761